

accepted 2026 01 22

Comprehensive Gaia DR3-Based Astrometric, Photometric, and Kinematic Studies of the Binary Open Cluster h and χ Persei

Seval Taşdemir¹, Waleed Elsanhoury², Deniz Cennet Çınar¹, Aly Haroon^{3,4}, and Selçuk Bılır^{5,*}

¹ Istanbul University, Institute of Graduate Studies in Science, Programme of Astronomy and Space Sciences, 34116, Beyazıt, İstanbul, Türkiye

² Northern Border University, College of Science, Department of Physics, Arar, Saudi Arabia

³ King Abdulaziz University, Faculty of Science, Astronomy and Space Science Department, Jeddah, Kingdom of Saudi Arabia

⁴ National Research Institute of Astronomy and Geophysics (NRIAG), Department of Astronomy, Cairo, Egypt

⁵ Istanbul University, Faculty of Science, Department of Astronomy and Space Sciences, 34119, Beyazıt, İstanbul, Türkiye; sbilar@istanbul.edu.tr

Abstract In the *Gaia* era, a comprehensive analysis of the binary open clusters NGC 869 (h Persei) and NGC 884 (χ Persei) system has been conducted to investigate its structural, astrophysical, kinematic, and Galactic orbital properties, along with its dynamical evolution. By applying the UPMASK algorithm to *Gaia* astrometric data for the estimation of cluster membership probabilities, it has been determined that 808 stars in NGC 869 and 707 stars in NGC 884 exhibit the highest statistical likelihood of being cluster members. The fundamental astrophysical parameters of the clusters were inferred within a Bayesian framework using *Gaia* data and PARSEC stellar evolutionary isochrones, through the application of the Markov Chain Monte Carlo (MCMC) technique. The estimated parameters are: colour excess $E(B-V) = 0.516^{+0.17}_{-0.24}$ mag and $0.516^{+0.22}_{-0.33}$ mag, distances 2376^{+301}_{-278} and 2273^{+230}_{-290} pc, ages $\log(t/\text{yr}) = 7.31^{+0.17}_{-0.32}$ and $\log(t/\text{yr}) = 7.30^{+0.13}_{-0.29}$, and metallicities $[\text{Fe}/\text{H}] = -0.24 \pm 0.12$ and $[\text{Fe}/\text{H}] = -0.25 \pm 0.12$ dex for NGC 869 and NGC 884, respectively. Since spectroscopic observations are not available for the clusters, SED analysis was employed for the member stars, yielding results consistent with those obtained using the MCMC method. Kinematic and Galactic orbital analyses suggest that the open clusters originated in nearby regions of the Galaxy. This interpretation is supported by their similar space velocities and Galactic orbital parameters. Furthermore, orbital integration over 1 Gyr indicates a potential interaction between the clusters within the next 11 Myr. This study provides strong evidence of a common origin and a possible future dynamical interaction, contributing valuable insights into the formation and evolution of binary open clusters in the Milky Way.

*Corresponding author, sbilar@istanbul.edu.tr

Key words: Galaxy: open cluster and associations: individual: NGC 869 and NGC 884, stars: Hertzsprung-Russell (HR) diagram, Galaxy: Stellar kinematics

1 INTRODUCTION

Open clusters (OCs) are key tracers of the Galactic disc's structure, chemical evolution, and formation properties. They serve as fundamental laboratories for testing stellar evolution theories due to their relatively uniform ages and chemical compositions. While most OCs are found as single stellar groupings, a fraction appear in binary or multiple cluster systems, which can provide deeper insights into cluster formation mechanisms and dynamical evolution. Binary OCs (BOCs) offer key evidence that star clusters can form and evolve through interactions beyond isolated conditions. Based on a statistical analysis, de La Fuente Marcos & de La Fuente Marcos (2009) emphasized that the occurrence and properties of such pairs help constrain the models of clustered star formation and early dynamical evolution.

Recent studies have identified several OCs located nearby and potentially exhibiting mutual gravitational interactions (Vereshchagin et al. 2022; Song et al. 2022; Li & Zhu 2025; Haroon et al. 2024; Palma et al. 2025; Taşdemir & Çınar 2025). These systems, referred to as close binary open clusters (CBOCs), are of particular interest as they provide unique astrophysical laboratories for understanding the formation, evolution, and disruption of stellar clusters. CBOCs not only allow researchers to trace the early conditions of star formation but also offer valuable insight into how clusters dynamically interact with each other and respond to the large-scale potential of the Milky Way (MW). As such, investigating these rare systems has become increasingly significant in the broader context of Galactic structure and star cluster evolution. BOCs are typically identified based on three primary criteria, namely spatial proximity, similar ages, coherent proper motions, and radial velocities. These systems are thought to originate from the fragmentation of the same giant molecular cloud (Fujimoto & Kumai 1997) or through tidal capture processes (Camargo 2021). BOCs studies allow us to explore whether such pairs are physically bound or merely line-of-sight coincidences.

NGC 869 (η Persei) and NGC 884 (χ Persei), are two prominent and spatially close clusters that constitute the well-known BOC in Perseus. NGC 869 and NGC 884 are classified as Trumpler type I3r, indicating that they are rich clusters with a strong central concentration and a wide range of stellar magnitudes (Ruprecht 1966). The equatorial coordinates of NGC 869 and NGC 884 are $\alpha = 02^{\text{h}}18^{\text{m}}57^{\text{s}}.84$, $\delta = +57^{\circ}08'02''.4$ and $\alpha = 02^{\text{h}}22^{\text{m}}20^{\text{s}}.16$, $\delta = +57^{\circ}08'56''.4$ (J2000.0), respectively. These correspond to Galactic coordinates of $(l, b) = (134^{\circ}.6257, -3^{\circ}.7372)$ for NGC 869 and $(135^{\circ}.0552, -3^{\circ}.5683)$ for NGC 884. Also, NGC 869 and NGC 884 are well-known BOCs frequently referenced in the literature due to their spatial proximity and similar astrophysical properties. The advent of the *Gaia* mission (Gaia Collaboration et al. 2016), with its unprecedented astrometric and photometric precision, has made it possible to re-examine these OCs in greater detail. Such high-quality data is essential for refining our understanding of their dynamical relationship, origin, and evolutionary status within the Galactic disc. The most prominent and widely studied CBOCs in the MW are the NGC 869 and NGC 884. They are located at a heliocentric distance of 2.3-2.4 kpc, and both OCs exhibit remarkable similarities in age, kinematics, and stellar population characteristics (Bragaglia et al. 2001; Currie et al. 2010; Cantat-Gaudin et al. 2020). Both ages are typically estimated between 12 and 15 Myr (Marco et al. 2001), and the OCs are among the most massive young OCs known in the MW.

In this study, we perform a photometric and kinematic analysis of NGC 869 and NGC 884 using *Gaia* DR3 data to investigate their structural parameters, membership, kinematics, and Galactic orbits, and to assess their physical association and formation history. Section 2 presents the astrometric and photometric data, while Section 3 outlines the methods and main results. Section 4 discusses the clusters' kinematical and dynamical properties, and Section 5 examines their dynamical parameters and mass distributions. Finally, Section 6 discusses the obtained results in comparison with previous studies in the literature and summarises the main conclusions regarding the evolutionary status of both OCs.

2 DATA

The photometric, astrometric, and spectroscopic data used in this study were obtained from the *Gaia* DR3 catalogue (Gaia Collaboration et al. 2023). The photometric data include G , G_{BP} , and G_{RP} magnitudes, while the astrometric parameters comprise the equatorial coordinates (α, δ) , trigonometric parallax (ϖ), and proper-motion components $(\mu_\alpha \cos \delta, \mu_\delta)$. Additionally, radial velocity (V_{R}) measurements derived from *Gaia* spectroscopic data were also used in the analysis, when available. All parameters, along with their associated uncertainties, were used in the analysis. 95,454 stellar sources were obtained from the *Gaia* DR3 database within a 40 arcminute radius centred at $\alpha = 02^{\text{h}}20^{\text{m}}39^{\text{s}}.12$, $\delta = +57^{\circ}08'31''.2$, encompassing the BOCs NGC 869 and NGC 884. Various filtering criteria were applied to increase the reliability of the data and to eliminate astrometrically problematic sources. A total of 9,374 sources were eliminated from the dataset because they lacked a Renormalised Unit Weight Error (RUWE) value. According to Lindegren et al. (2021), sources with RUWE values around 1 demonstrate good agreement with the single-star model. In contrast, RUWE values of 1.4 (Castro-Ginard et al. 2024) and above generally indicate binary stars or problematic sources for the astrometric solution. In this particular context, 2,975 stars with $\text{RUWE} \geq 1.4$ were also eliminated due to their low accuracy. Among these, 1,829 stars were found to have G -band magnitudes brighter than $G = 17$, suggesting that the astrometric quality may degrade significantly at fainter magnitudes. In addition, 517 stars bearing the `duplicate_source` flag were eliminated from the dataset; 76 of these stars were subsequently identified as exhibiting high RUWE values. As a result of the applied filtering steps, a final, reliable sample of 92,038 stars was obtained and subsequently analysed in detail.

Additionally, an identification chart was created to provide a comprehensive spatial view of the system. This diagram utilizes the $80' \times 80'$ arcminutes of space in which both OCs are located, clearly showing the individual clusters and their positions relative to each other. The identification chart based on this field is demonstrated in Figure 1, where NGC 869 and NGC 884 are distinctly visible.

3 DATA ANALYSES

3.1 Photometric Completeness Limit

Accurate determination of structural and astrophysical parameters for both OCs requires establishing their photometric completeness limits. This procedure is vital for minimising potential biases in subsequent analyses. For each OC, the stellar number distributions were examined across different *Gaia* G -band apparent magnitude intervals. As shown in Figure 2, star counts increase with fainter magnitudes up to a peak near

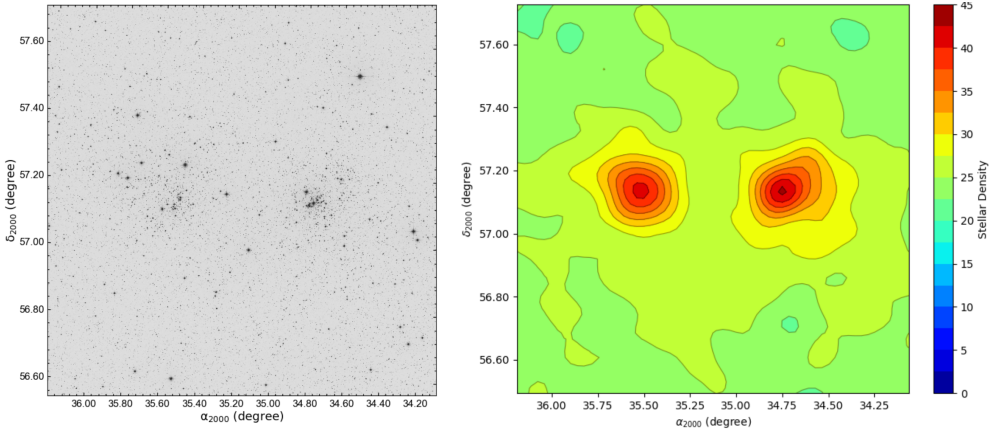


Fig. 1: Finder chart of the region containing the BOCs NGC 869 and NGC 884, obtained from the STScI Digitized Sky Survey (DSS). The red dashed circle indicates the area analyzed (left panel). Stellar surface density map of the same region, revealing two significant overdensities corresponding to NGC 869 (a) and NGC 884 (b) (right panel). Warmer colours represent higher stellar densities.

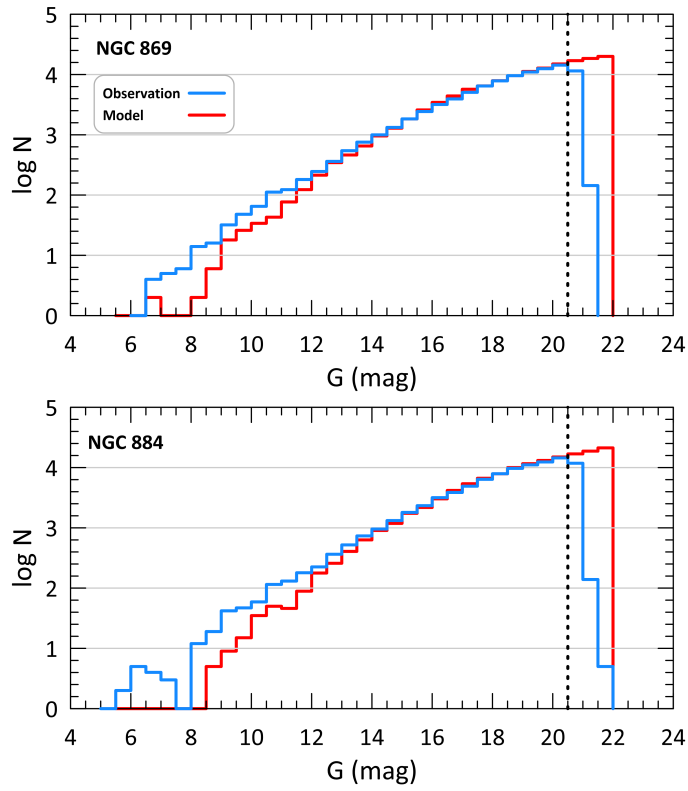


Fig. 2: The G –band star count histograms for NGC 869 and NGC 884 are presented, where the observational data are shown in black and the model predictions in red; the black dashed lines denote the photometric completeness limits.

$G = 20.5$ mag. Beyond that magnitude limit, the number of detected sources declines, indicating the point at which the data becomes incomplete.

To assess the photometric completeness levels, synthetic stellar samples were generated for the fields of both OCs using the Besançon Galaxy Model¹ (Robin et al. 2003), which incorporates the three-dimensional extinction map of Marshall et al. (2006) and thus provides realistic extinction conditions along the relevant lines of sight. The simulations, carried out over the magnitude range $5 < G$ (mag) ≤ 22 , were designed to reproduce the distribution of the observed star counts and employed solid angles of 0.445 deg 2 for each cluster region. Comparison of the synthetic and observed star distributions (Figure 2) shows that the excess of observed stars at bright G magnitudes represents the magnitude domain in which cluster stars are fully sampled, whereas magnitudes at which the model begins to overpredict the observations define the photometric completeness limits. This evaluation confirms that the present data exhibit no loss of completeness, consistent with previous findings. Therefore, the completeness G –band apparent magnitudes of both OCs examined in this study were adopted as 20.5 mag.

To estimate photometric uncertainties, the errors provided in the *Gaia* DR3 catalogue were considered as interval-based uncertainties. Within defined G -band apparent magnitude bins, the mean G -band apparent magnitudes and corresponding $G_{\text{BP}} - G_{\text{RP}}$ colour indices of stars located in the OCs region were computed. At the photometric completeness limit of $G = 20.5$ mag, the mean internal uncertainty in the G -band apparent magnitude was determined to be 0.007 mag, while the mean uncertainty in the $G_{\text{BP}} - G_{\text{RP}}$ colour index was found to be 0.107 mag. A detailed overview of the mean photometric errors across the G magnitude range for both OCs is listed in Table 1.

These calculations are particularly important as the *Gaia* EDR3/DR3 photometric uncertainties represent a general calibration model based on an all-sky survey (Riello et al. 2021), which may not fully reflect local observing conditions such as crowding and background contamination in dense cluster regions. An inspection of our internal errors reveals that in the apparent magnitude range of $G < 18$, the mean uncertainty is $\sigma_G \approx 0.003$ mag, which remains close to the nominal precision limits presented by Riello et al. (2021). At the faint end ($G > 20$ mag), however, errors increase more rapidly ($\sigma_G \approx 0.009 - 0.027$ mag) compared to the all-sky average due to the expected crowding effect. Notably, the uncertainty in the $G_{\text{BP}} - G_{\text{RP}}$ colour index reaches ~ 0.2 mag at the limit of $G > 20$ mag, which is consistent with the trends in Riello et al. (2021) and justifies the careful treatment of this limit for isochrone fitting.

3.2 Structural Parameters

To characterise the spatial distribution and structural properties of NGC 869 and NGC 884, a radial density profile (RDP) analysis was performed. The area surrounding each OC was partitioned into a series of concentric annuli, with the OC center as the origin. For each annulus, the surface stellar density $\rho(r)$ was computed using the relation $R_i = N_i/A_i$, where N_i is the number of stars contained within the i^{th} ring and A_i is the corresponding area. All annuli were defined such that their outer radii satisfy $r \leq 40'$, ensuring that each ring lies entirely within the selected region and has a complete, well-defined area. Only stars brighter than the photometric completeness limit of $G = 20.5$ mag were included in the calculation to avoid biases due to incompleteness.

¹ <https://model.obs-besancon.fr/>

Table 1: Photometric uncertainties in G -band apparent magnitudes and $G_{\text{BP}} - G_{\text{RP}}$ colour indices for stars located in the cluster field.

G (mag)	N	σ_G (mag)	$\sigma_{G_{\text{BP}} - G_{\text{RP}}}$ (mag)
(5, 12]	392	0.003	0.006
(12, 14]	1,393	0.003	0.005
(14, 15]	1,788	0.003	0.005
(15, 16]	3,420	0.003	0.006
(16, 17]	5,954	0.003	0.010
(17, 18]	9,666	0.003	0.017
(18, 19]	15,536	0.003	0.038
(19, 20]	21,579	0.004	0.080
(20, 21]	28,442	0.009	0.206
(21, 22]	3,869	0.027	0.446

The radial distribution of stellar density was derived by counting stars at successive angular distances from the cluster center, aiming to determine the structural properties of the OCs in this study. The King profile was adopted for the RDP analysis, as it is widely used in the literature owing to its empirical success in describing the stellar density distribution from the cluster center to its outskirts (King 1962), and its effectiveness in deriving key structural parameters such as the core and limiting radii (Bonatto & Bica 2005). The observed RDPs were compared with King (1962) and the structural parameters of the OCs were determined. The King profile model is described as follows:

$$\rho(r) = f_{\text{bg}} + \frac{f_0}{1 + (r/r_c)^2}, \quad (1)$$

where r denotes the radial distance, r_c is the core radius, f_0 is the central stellar density, and f_{bg} is the background field star density. A chi-squared minimization technique was employed to identify the optimal model parameters, with the final estimates corresponding to the values that minimize the χ^2 . An examination of the RDP yielded an observed limiting radius, $r_{\text{lim}}^{\text{obs}}$, of approximately 20'. The estimated structural parameters obtained from the King model fitting for each OC are illustrated in Figure 3, and the results are given in Table 2.

$$r_{\text{lim}} = r_c \sqrt{\frac{f_0}{3\sigma_{\text{bg}}} - 1}. \quad (2)$$

Applying this relation with our fitted parameters resulted in a theoretical limiting radius of $r_{\text{lim}} = 19.15 \pm 0.84$ and $r_{\text{lim}} = 19.52 \pm 0.32$ arcmin for NGC 869 and NGC 884, respectively. The close agreement between this theoretical estimate and the observed value supports the internal consistency and robustness of the derived structural parameters. When Figure 3 is investigated carefully, a bump in the stellar number density can be seen in the RDP of NGC 869 at a distance of 7-10 arcminutes from the OC center. This raises the question of whether stars belonging to the NGC 884 OC are mixing into NGC 869. The analyses related to this issue will become clearer after the cluster member stars are identified in Section 3.3 of this study.

In the structural characterisation of young and dense OCs such as NGC 869 and NGC 884 the density contrast parameter plays an important role in quantifying the degree of stellar concentration against the background field. Following the formulation introduced by Bica & Bonatto (2005), the density-contrast parameter is defined as $\delta_c = 1 + f_0/f_{\text{bg}}$, where f_0 and f_{bg} represent the central and background stellar

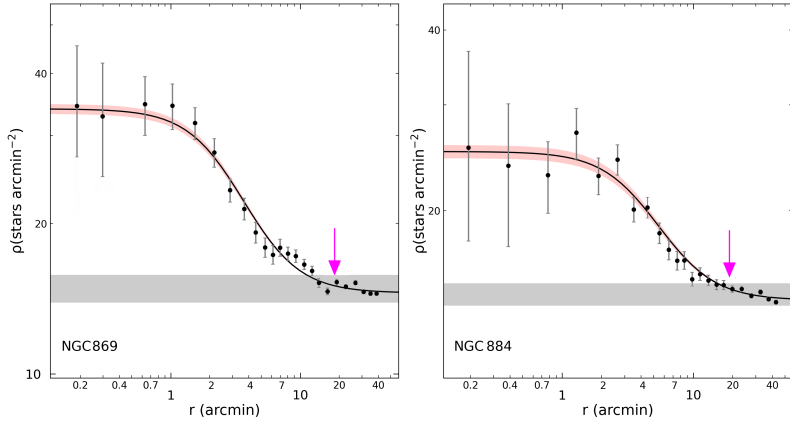


Fig. 3: RDPs for NGC 869 (left panel) and NGC 884 (right panel) with best-fit King models (black lines). The magenta arrows indicate the limiting radii; the gray bands show background density levels. The 1σ fitting uncertainty is shown as a red-shaded band around the King profile.

densities, respectively. In this study, the density-contrast parameters derived for NGC 869 ($\delta_c = 2.34 \pm 0.02$) and NGC 884 ($\delta_c = 1.77 \pm 0.05$) indicate relatively moderate central stellar concentrations in both OCs. For comparison, several Galactic OCs analysed in previous studies exhibit similarly low to moderate density-contrast values. For example, the density-contrast parameter calculated for NGC 188, which exhibits a relatively high central concentration, is $\delta_c = 21.5$ (Bonatto & Bica 2005). In contrast, Bica & Bonatto (2005), who analysed five OCs located in the third Galactic quadrant, reported density-contrast values ranging from $\delta_c = 6.4$ (Czernik 31) to $\delta_c = 11.2$ (Trumpler 13), highlighting that low to intermediate density-contrast values can also be observed among OCs. Similarly, Camargo et al. (2010) demonstrated that young and moderately populated OCs commonly present $\delta_c \lesssim 3$, reflecting relatively diffuse core structures. In this context, the density-contrast parameters obtained for NGC 869 and NGC 884 are consistent with those reported for other Galactic OCs. This suggests that both OCs may represent dynamically young systems or possess less centrally concentrated core structures compared to more compact stellar systems.

The concentration parameter ($C = r_{\text{tidal}}/r_c$) is an indicator of a cluster's internal structure and dynamical state, influenced by internal evolution and the Galactic environment. Although the classical definition uses the tidal radius (r_{tidal}) (King 1966), many studies instead adopt the limiting radius (r_{lim}) due to the difficulty of measuring r_{tidal} , a practical approach also used by Hill & Zaritsky (2006), Muñoz et al. (2010), and Miocchi et al. (2013). For NGC 869 and NGC 884, we obtain concentration parameters of 6.49 ± 1.13 and 4.14 ± 0.44 , respectively. These values are higher than the lower concentration limit typically found in dynamically young and weakly concentrated OCs, for which $C \simeq 2\text{-}3$ is commonly reported in the literature (e.g., Piskunov et al. 2007; Kharchenko et al. 2013). However, they remain below the concentrations characteristic of dynamically evolved systems, indicating that both OCs exhibit moderate central concentration consistent with their young ages and early-stage dynamical evolution. All structural parameters are also provided in Table 2.

Table 2: Structural parameters of NGC 869 and NGC 884 estimated from King model fitting.

Parameter	NGC 869	NGC 884
r_c (arcmin)	2.95 ± 0.26	4.71 ± 0.60
r_c (pc)	2.04 ± 0.18	3.11 ± 0.40
r_{lim} (arcmin)	19.15 ± 0.84	19.52 ± 0.32
r_{lim} (pc)	13.24 ± 0.59	12.90 ± 0.21
f_0 (stars arcmin $^{-2}$)	19.43 ± 0.26	10.91 ± 0.64
f_{bg} (stars arcmin $^{-2}$)	14.52 ± 0.15	14.18 ± 0.20
δ_c	2.34 ± 0.02	1.77 ± 0.05
C	6.49 ± 1.13	4.14 ± 0.44

3.3 Membership Determination

A reliable characterisation of the astrophysical parameters of NGC 869 and NGC 884 requires an accurate identification of their stellar members, particularly given their location in the dense stellar fields of the Galactic plane, where field-star contamination is significant. Since genuine OC members are coeval and share common kinematic properties, such as proper motions and parallaxes, these features provide a robust basis for distinguishing them from foreground and background stars. To identify probable cluster members, we employed the Unsupervised Photometric Membership Assignment in Stellar Clusters (UPMASK) algorithm (Krone-Martins & Moitinho 2014). This method is designed to determine cluster membership probabilities by combining positional and photometric information without requiring prior assumptions about the underlying distributions. UPMASK operates through an iterative process that utilizes k -means clustering and statistical resampling to assess the spatial coherence of stellar groups in multi-dimensional parameter space. It is particularly effective for OCs observed by *Gaia*, as it allows for robust member selection even in crowded fields and in the presence of field star contamination.

In this study, we used the UPMASK methodology to perform a detailed membership analysis for both OCs. The analysis employed astrometric data from the *Gaia* DR3 catalogue, including equatorial coordinates (α, δ) , proper-motion components $(\mu_\alpha \cos \delta, \mu_\delta)$, and trigonometric parallaxes (ϖ) , together with their associated uncertainties. UPMASK identifies statistically significant clustering of stars consistent with the expected distribution of cluster members by applying the k -means clustering algorithm in a multidimensional parameter space. The optimal number of k -means clusters was determined by examining the stability of the resulting membership probabilities for different k values. Cluster memberships corresponding to the value at which probabilities no longer changed significantly with increasing k were adopted. Based on this criterion, we selected $k = 27$ for NGC 869 and $k = 28$ for NGC 884, ensuring transparency and robustness in the k -means configuration. Due to its effectiveness, UPMASK is widely employed in the literature for determining cluster membership (e.g., Cantat-Gaudin et al. 2018a; Castro-Ginard et al. 2018; Cantat-Gaudin et al. 2020; Akbulut et al. 2021; Yontan et al. 2021, 2022; Wang et al. 2022; Yontan 2023; Karagöz et al. 2025).

A total of 92,038 stars within the defined search radius around both OCs were initially considered. After filtering based on astrometric precision and photometric completeness (limiting magnitude $G \leq 20.5$ mag), the UPMASK algorithm was executed, assigning membership probabilities in the range $0 \leq P \leq 1$ to the

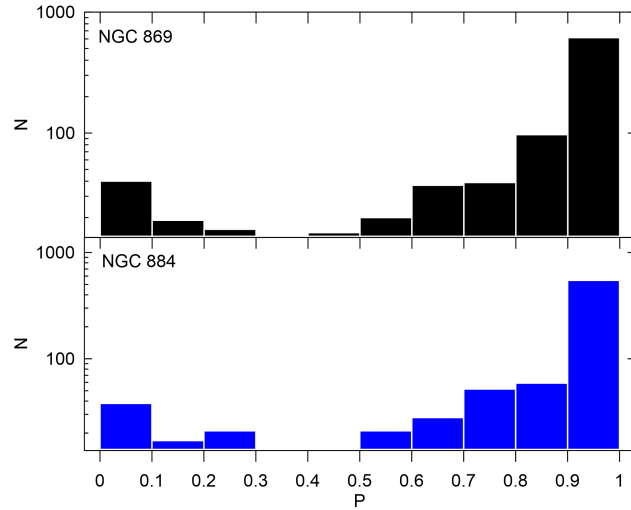


Fig. 4: Distribution of membership probabilities assigned by the UPMASK algorithm for stars in the directions of the NGC 869 and NGC 884.

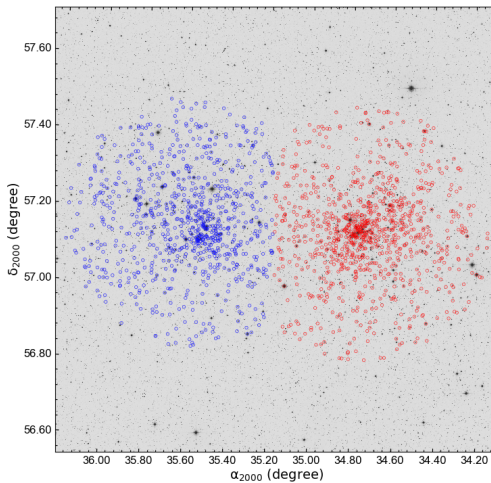


Fig. 5: Sky chart showing the spatial distribution of members for NGC 869 (black) and NGC 884 (red). The background image is taken from the STScI DSS.

remaining stars. The membership probability distributions for both OCs are shown in Figure 4, revealing a clear excess of high-probability stars compared to the field-star baseline, with the majority of stars exhibiting probabilities greater than $P = 0.5$. Based on these probabilities, 808 and 707 stars were classified as probable members ($P \geq 0.5$) of NGC 869 and NGC 884, respectively. Only stars satisfying the criterion $P \geq 0.5$ were retained for all subsequent analyses presented in the following sections of this study.

Figure 5 shows the sky positions of stars with membership probabilities $P \geq 0.5$ for both OCs. The stars tested for dual membership exhibit almost no spatial overlap, indicating that there is no population contamination between the OCs. This finding demonstrates that the bump-like feature observed in Figure 3 at a distance of 7-10 arcmin from the center of the NGC 869 is not caused by contamination from member stars of NGC 884. Instead, it originates from the spatial distribution of field stars along the line of sight toward the OC.

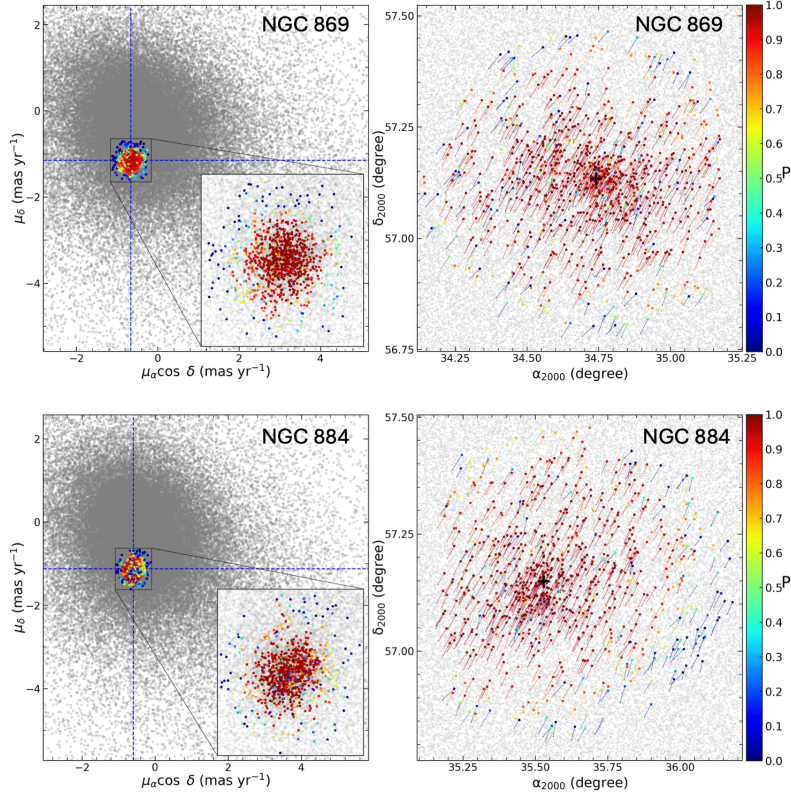


Fig. 6: The panels show the VPDs and moving vectors of the OC members on the equatorial-coordinate plane, respectively, for the NGC 869 (upper panels) and NGC 884 (lower panels). Colour-scaled circles and vectors indicate the likely cluster members and their corresponding movement directions. The zoomed-in boxes in the VPDs indicate the distribution of the OCs according to field stars (gray circles). The intersection of black dashed lines (left panels) indicates the mean proper-motion values, whereas the black plus symbols represent the center of the OCs on the equatorial coordinate planes.

3.4 Astrometric Parameters

To further investigate the kinematic coherence of the identified members, we constructed vector point diagrams (VPDs) for both OCs, shown in Figure 6. These diagrams illustrate the proper-motion components ($\mu_\alpha \cos \delta, \mu_\delta$) distribution of stars in the VPD. In both cases, the OCs manifest as compact overdensities that are distinguishable from the surrounding star field population. The mean proper-motion components were estimated using stars with $P \geq 0.5$, yielding $(\mu_\alpha \cos \delta, \mu_\delta) = (-0.662 \pm 0.022, -1.150 \pm 0.027) \text{ mas yr}^{-1}$ for NGC 869 and $(-0.593 \pm 0.025, -1.128 \pm 0.028) \text{ mas yr}^{-1}$ for NGC 884. These results are consistent with previous findings in the literature (c.f. Cantat-Gaudin et al. 2020; Hunt & Reffert 2024), thereby reinforcing the reliability of the membership determination process. Furthermore, we analysed the *Gaia*-based trigonometric parallax values of the confirmed member stars in NGC 869 and NGC 884.

The mean trigonometric parallaxes of both OCs were determined by analysing the distribution of cluster member stars with relative parallax error $\sigma_\varpi / \varpi \leq 0.2$ in the trigonometric parallax versus magnitude ($\varpi \times G$) diagram in Figure 7. Under the applied constraints, 728 and 624 stars were identified as likely members of NGC 869 and NGC 884, respectively. These stars have reliably measured trigonometric parallaxes and are detected down to a limiting magnitude of $G = 17.5$. As can be seen from Figure 7, the cluster members span

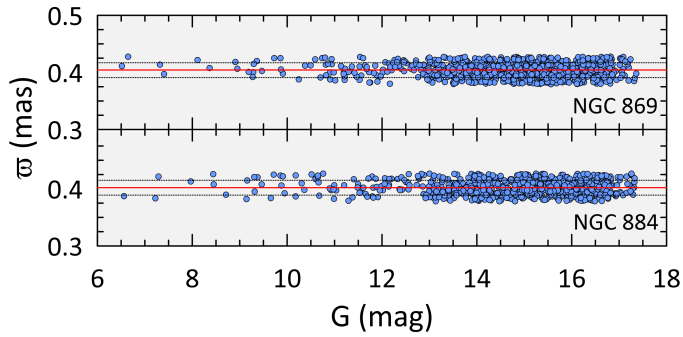


Fig. 7: Positions of OC member stars with $\sigma_{\varpi}/\varpi \leq 0.2$ in the $\varpi \times G$ diagrams. The red line indicates the median trigonometric parallax of the stars, while the black dashed lines represent the $\pm 1\sigma$ deviation from the median values.

a wide range of magnitudes while being concentrated around similar ϖ values, supporting their membership in the respective cluster. The analysis indicates that the median trigonometric parallaxes of the NGC 869 and NGC 884, respectively, are 0.404 ± 0.013 and 0.402 ± 0.013 mas. To convert these parallax values into heliocentric distances, we used the relation $d(\text{pc}) = 1000/\varpi$ (mas). Accordingly, the distances were computed as $d_{\varpi} = 2475 \pm 80$ pc for NGC 869 and $d_{\varpi} = 2488 \pm 80$ pc for NGC 884.

In this study, the trigonometric parallax values calculated for the NGC 869 and NGC 884 were compared with those reported in previous studies based on *Gaia* DR2 and *Gaia* DR3 astrometric data. Cantat-Gaudin et al. (2020) reported trigonometric parallax values of 0.399 ± 0.042 mas and 0.398 ± 0.038 mas, while Dias et al. (2021) provided estimates of 0.400 ± 0.043 mas and 0.398 ± 0.039 mas for the NGC 869 and NGC 884, respectively. In this study, the use of *Gaia* DR3 data enabled the estimation of trigonometric parallax values with uncertainties approximately three times smaller than early *Gaia* DR2 studies, and also our findings are in agreement with recent studies such as Hunt & Reffert (2024) reported values of 0.404 ± 0.019 mas and 0.402 ± 0.019 mas.

3.5 Astrophysical Parameters Estimation

To estimate the fundamental parameters of both OCs, we employed two independent and complementary approaches. The first is a Bayesian framework based on Markov Chain Monte Carlo (MCMC) sampling, applied to *Gaia*-based colour-magnitude diagrams (CMDs). This method allows the simultaneous exploration of the parameter space, including reddening, distance modulus, metallicity, and age, while fully accounting for observational uncertainties and parameter degeneracies. The posterior distributions obtained through MCMC provide statistically rigorous constraints on the clusters' astrophysical properties. The second method utilises spectral energy distribution (SED) fitting, incorporating multi-band photometry to model the observed fluxes of cluster member stars. By comparing the results obtained from both techniques, we aim to achieve a more robust and consistent characterization of the OCs' astrophysical properties.

3.5.1 MCMC Simulations

The estimation of the fundamental parameters for NGC 869 and NGC 884 was carried out through the construction and analysis of CMDs, which are powerful diagnostics in OC studies (see also, Bilir et al. 2006;

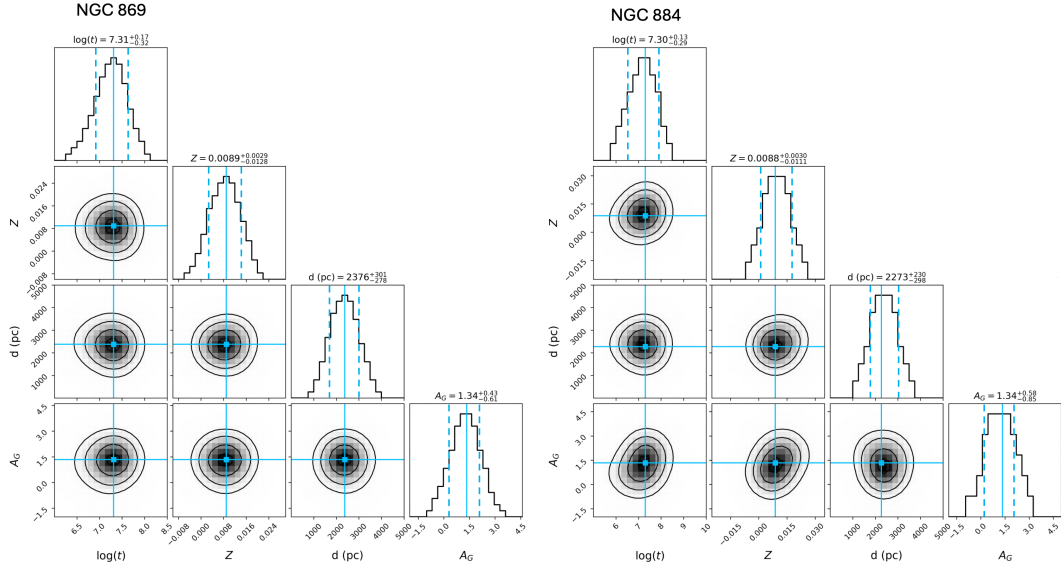


Fig. 8: Corner diagram illustrating the posterior distributions of the inferred astrophysical parameters for NGC 869 and NGC 884 derived from the MCMC analysis. The solid black lines mark the median values of the parameters, whereas the dashed black lines indicate the corresponding 16th and 84th percentile confidence intervals.

Bilir et al. 2010; Bilir et al. 2016; Bostancı et al. 2015, 2018; Yontan et al. 2015, 2019; Ak et al. 2016; Banks et al. 2020; Koç et al. 2022). These diagrams clearly display evolutionary sequences, such as the main sequence (MS) and turn-off point, enabling precise determination of cluster parameters.

Precise constraints on key astrophysical quantities such as cluster age, chemical composition, distance modulus, and line-of-sight extinction are crucial for interpreting the formation pathways and evolutionary stages of OCs. To obtain these parameters in a self-consistent way, we applied a Bayesian framework based on a MCMC technique, following the methodology outlined by Tanık Öztürk et al. (2025), coupled with the PARSEC stellar evolutionary models (Bressan et al. 2012). Within this framework, the MCMC sampler explores the joint posterior distribution of the model parameters under the assumption of Gaussian observational uncertainties. The logarithmic likelihood function, adapted from Tanık Öztürk et al. (2025), is expressed in Equation (3):

$$\ln \mathcal{L}(\theta) = \sum_{i=1}^{N_{\text{stars}}} \sum_X \left[\frac{(m_{X,i} - \hat{m}X, i)^2}{2\sigma_{X,i}^2} \ln(\sqrt{2\pi}, \sigma_{X,i}) \right], \quad (3)$$

where $m_{X,i}$ denotes the observed magnitudes in the G , G_{BP} , and G_{RP} passbands, $\hat{m}X, i$ corresponds to the model predictions from the stellar grid, $\sigma_{X,i}$ represents the photometric uncertainties, and θ contains the parameters of interest (log(age), A_G , distance, and metallicity). The analysis incorporates the high-probability members of each cluster, ensuring that the posterior distribution reflects the intrinsic cluster properties as closely as possible. To efficiently sample this posterior, we employed the `emcee` ensemble sampler (Foreman-Mackey et al. 2013), assigning one walker per most-probable member star. Each chain was evolved over 5,000 iterations, ensuring adequate convergence. The resulting posterior distributions were used to derive the best-fitting parameter estimates and their associated 1σ uncertainties in Figure 8, and the fundamental parameters calculated for the OCs are listed in Table 3.

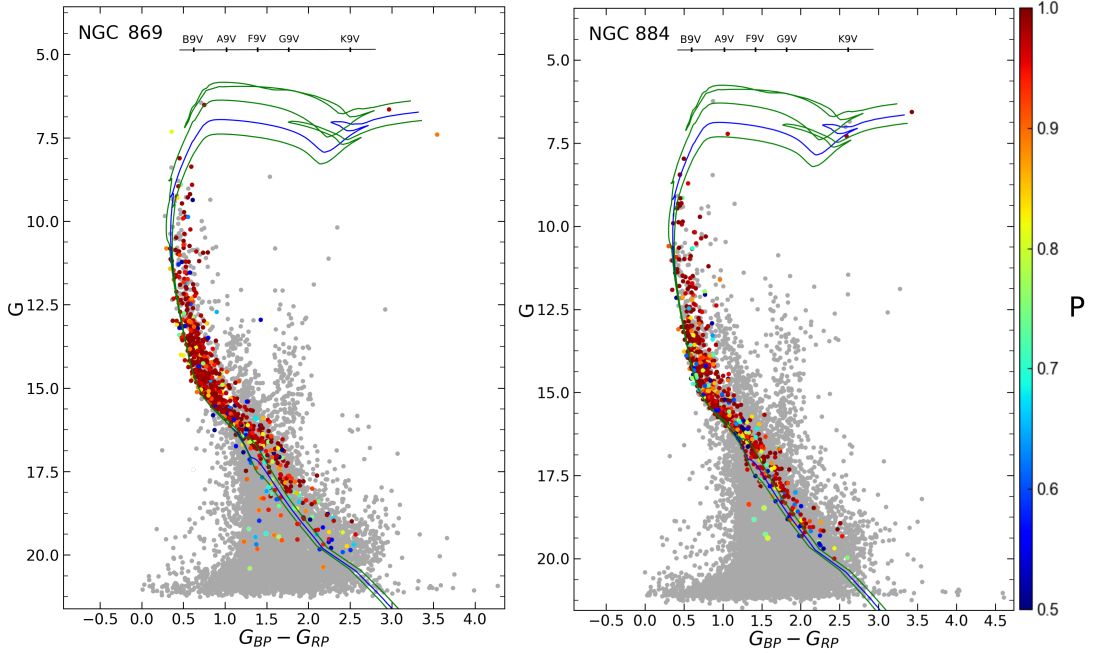


Fig. 9: CMDs of NGC 869 and NGC 884 showing OC members. Stars with $0.5 \leq P \leq 1$ are shown in different colour codes, and field stars are displayed in grey circles. The best-fitting PARSEC isochrones (black) and their associated uncertainty ranges (green) correspond to the ages derived for both OCs. Spectral type classes of the stars are shown along the top axis of the CMDs, following the classification scheme of Pecaut & Mamajek (2013).

Using the fundamental parameters such as G -band extinction, distance, metallicity, and age obtained via the MCMC method, theoretical isochrones from the PARSEC database (Bressan et al. 2012) were fitted to the observed CMDs of both OCs. Stars with high-cluster membership probabilities and field stars along the line of sight to the OCs were marked on the $G \times (G_{BP} - G_{RP})$ CMDs constructed from *Gaia* photometry, and the corresponding PARSEC isochrones based on the parameters derived using the MCMC method were overplotted in Figure 9. In addition, spectral types of stars, adapted schematically from Pecaut & Mamajek (2013), are also shown on the CMDs. An examination of the positions of cluster member stars fitted with PARSEC isochrones reveals that both OCs contain early-type stars. Additionally, the presence of pre-main-sequence stars, which have not yet reached the main sequence, is noteworthy. This finding provides supporting evidence for the young ages of the OCs. Furthermore, considering the spectral type classifications given by Pecaut & Mamajek (2013), it has been determined that the stars approaching the main sequence are approximately of early F-spectral type.

From the colour excesses, the corresponding extinction values in the G band were computed using $A_G = 1.8626 \times E(G_{BP} - G_{RP})$. These *Gaia*-based colour excesses and extinction estimates were subsequently transformed into the UBV photometric system through the relations $E(G_{BP} - G_{RP}) = 1.41 \times E(B - V)$ and $A_G = 0.83626 \times A_V$ (Canbay et al. 2023). The apparent distance moduli obtained from the posterior distributions correspond to MCMC-inferred distances of 2376^{+301}_{-278} pc for NGC 869 and 2273^{+230}_{-298} pc for NGC 884.

Table 3: The fundamental parameters determined for both OCs in this study via MCMC and SED methods.

Parameter	NGC 869	NGC 884
Astrometric Parameters		
$(\alpha, \delta)_{\text{J2000}}$	02:18:57.84, +57:08:02.40	02:22:20.16, +57:08:56.40
$(l, b)_{\text{J2000}} (\text{deg})$	134.6257, -3.7372	135.0552, -3.5683
Number of members	808	707
$\mu_\alpha \cos \delta (\text{mas yr}^{-1})$	-0.662 ± 0.022	-0.593 ± 0.025
$\mu_\delta (\text{mas yr}^{-1})$	-1.150 ± 0.027	-1.128 ± 0.028
$\varpi (\text{mas}) (\sigma_{\varpi}/\varpi \leq 0.2)$	$0.404 \pm 0.013 (N=728)$	$0.402 \pm 0.013 (N=624)$
$d_{\varpi} (\text{pc})$	2475 ± 80	2488 ± 80
$V_{\text{R}} (\text{km s}^{-1})$	$-38.17 \pm 3.23 (N=13)$	$-40.21 \pm 2.95 (N=14)$
Astrophysics Parameters - MCMC method		
Number of members	808	707
$E(B - V) (\text{mag})$	$0.516_{-0.24}^{+0.17}$	$0.516_{-0.33}^{+0.22}$
$E(G_{\text{BP}} - G_{\text{RP}}) (\text{mag})$	$0.72_{-0.33}^{+0.23}$	$0.72_{-0.46}^{+0.31}$
$A_{\text{G}} (\text{mag})$	$1.34_{-0.61}^{+0.43}$	$1.34_{-0.85}^{+0.58}$
$[\text{Fe}/\text{H}] (\text{dex})$	-0.24 ± 0.12	-0.25 ± 0.12
Z	$0.0089_{-0.0128}^{+0.0029}$	$0.0088_{-0.0111}^{+0.0031}$
$(G - M_{\text{G}}) (\text{mag})$	$13.22_{-0.88}^{+0.68}$	$13.12_{-1.15}^{+0.79}$
$d_{\text{iso}} (\text{pc})$	2376_{-278}^{+301}	2273_{-298}^{+230}
$\log(t/\text{yr})$	$7.31_{-0.32}^{+0.17}$	$7.30_{-0.29}^{+0.13}$
Astrophysics Parameters - SED method		
Number of stars	349	286
$E(B - V) (\text{mag})$	0.484 ± 0.032	0.481 ± 0.032
$A_{\text{V}} (\text{mag})$	1.50 ± 0.10	1.49 ± 0.10
$[\text{Fe}/\text{H}] (\text{dex})$	-0.25 ± 0.03	-0.25 ± 0.03
$(V - M_{\text{V}}) (\text{mag})$	13.381 ± 0.123	13.279 ± 0.129
$d_{\text{SED}} (\text{pc})$	2378 ± 25	2279 ± 31
Z	0.0088 ± 0.0009	0.0088 ± 0.0009
$\log(t/\text{yr})$	7.30 ± 0.09	7.30 ± 0.09

The relation provided by Bovy² was used to convert the heavy-element abundances of the OCs into iron abundances ($[\text{Fe}/\text{H}]$), and it is calibrated for PARSEC stellar isochrones (Bressan et al. 2012). This relation has been successfully applied in several previous studies (e.g., Gokmen et al. 2023; Yontan et al. 2023; Yontan & Canbay 2023; Çakmak et al. 2024). In this approach, an intermediate variable Z_x is first computed as:

$$Z_x = \frac{Z}{0.7515 - 2.78 \times Z} \quad (4)$$

followed by the calculation of the OC iron abundances:

$$[\text{Fe}/\text{H}] = \log(Z_x) - \log\left(\frac{Z_{\odot}}{1 - 0.248 - 2.78 \times Z_{\odot}}\right) \quad (5)$$

In these expressions, $Z_{\odot} = 0.0152$ denotes the solar metallicity. The heavy-element abundances estimated using the MCMC method were converted into iron abundances via Equations 4 and 5, yielding metallicities ($[\text{Fe}/\text{H}]$) of -0.24 ± 0.12 and -0.25 ± 0.12 dex for NGC 869 and NGC 884, respectively.

For the NGC 869 and NGC 884, the colour excesses determined in the *Gaia* photometric system were transformed into the *UBV* system using the relations provided by Canbay et al. (2023), yielding

² <https://github.com/jobovy/isodist/blob/master/isodist/Isochrone.py>

$E(B - V) = 0.516_{-0.24}^{+0.17}$ and $E(B - V) = 0.516_{-0.33}^{+0.22}$ mag, respectively. These results are in agreement with those reported in the literature. In particular, Dias et al. (2021) derived values of $E(B - V) = 0.564 \pm 0.012$ mag for NGC 869 and 0.551 ± 0.006 mag for NGC 884, which are consistent with our findings within the quoted uncertainties. Moreover, Zhong et al. (2020) reported colour excess of $E(B - V) = 0.52$ mag for both OCs, further supporting the reliability of our estimates.

In this study, it is found that the distances calculated using the trigonometric parallax method for both OCs differ by 99–215 pc compared to those calculated using the MCMC method (see Table 3). This discrepancy becomes particularly significant for astronomical objects located beyond 2 kpc and is mainly caused by biases in the stellar trigonometric parallax measurements. As demonstrated by Plevne et al. (2020), this effect can be clearly seen by comparing *Gaia* trigonometric parallax data with the bias-corrected distances of Bailer-Jones et al. (2018) at distances of approximately 2 kpc from the Sun. In this study, the distances of both OCs derived from trigonometric parallaxes (~ 2.5 kpc) are measured to be, on average, $\cong 200$ pc closer than those obtained using a Bayesian approach. This explains the differences between the distances derived using the two different methods in this study. For the reasons stated above, the distances calculated using the MCMC method are adopted in this study. The distances estimated for both OCs in this study show general consistency with values reported in recent literature. For instance, Hunt & Reffert (2024) reported distances of 2279 ± 6 pc and 2293 ± 7 pc for NGC 869 and NGC 884, respectively. Similarly, Dias et al. (2021) obtained distances of 2246 ± 64 pc and 2150 ± 103 pc for NGC 869 and NGC 884, respectively, which are consistent within the uncertainties. In addition, Zhong et al. (2020) estimated distances of 2300 pc for NGC 869 and 2200 pc for NGC 884, providing further support to our derived values.

The metallicity adopted for both OCs in this study, $[Fe/H] \cong -0.25 \pm 0.12$ dex, is consistent with the limited spectroscopic constraints available for NGC 869 and NGC 884. Although high-resolution spectroscopic analyses for those clusters are scarce, large-scale spectroscopic surveys such as LAMOST provide statistically robust metallicity estimates. For example, Zhong et al. (2020) reported mildly subsolar metallicities for both clusters based on LAMOST DR5 spectra, supporting our adopted value. While these survey-based measurements are not high-resolution abundance analyses, they offer the most direct observational constraints currently available, and our metallicity assumption aligns well with these results.

The estimated logarithmic ages of $\log(t/\text{yr}) \cong 7.30 \pm 0.15$ for both OCs are also consistent with literature values. For example, Dias et al. (2021) reported $\log(t/\text{yr}) = 7.11 \pm 0.04$ for NGC 869 and 7.19 ± 0.05 for NGC 884, while other studies (e.g. Cantat-Gaudin et al. 2020; Song et al. 2022) suggest values within a similar range, corroborating the young age nature of both OCs. Additionally, Zhong et al. (2020) estimated an age of approximately 14 Myr for NGC 869 and 15 Myr for NGC 884, which are within the uncertainty limits of our results and confirm the coeval nature of both OCs.

3.5.2 Bayesian SED Modeling of OC Member Stars

A detailed SED analysis was conducted for the young both OCs using the ARIADNE Python package, a robust tool designed to perform Bayesian inference on stellar photometric data. This framework incorporates a suite of theoretical stellar atmosphere models, spanning a wide range of effective temperatures, surface gravities, and metallicities, which have been pre-convolved with an extensive set of standard photometric filter

transmission curves (Vines & Jenkins 2022). The sampling of the posterior probability distributions, as well as the estimation of the Bayesian evidence for competing models, was achieved through the implementation of the nested sampling algorithm provided by the `DYNESTY` library (Higson et al. 2019; Speagle 2020).

To build the broadband SEDs, we compiled all available photometry from the optical to the infrared regime and performed a careful cross-matching across surveys. We adopted the *Gaia* DR3 G , G_{BP} , and G_{RP} measurements (Gaia Collaboration et al. 2023) as the astrometric reference frame and matched them to 2MASS near-infrared data (J , H , K_s ; Skrutskie et al. 2006) using a $1''$ radius. Mid-infrared fluxes from *WISE* ($W1$ - $W4$; Wright et al. 2010) were added through a positional cross-match with typical separations $< 0''.5$, ensuring that only sources with clean photometric quality flags were retained. When available, Pan-STARRS1 and APASS measurements were incorporated to extend the spectral coverage and to reduce degeneracies in temperature and extinction.

The fitting procedure was executed in static mode, ensuring efficient exploration of the multi-dimensional parameter space without dynamic adjustment of the number of live points. We adopted a configuration of 500 live points, with the convergence criterion set to a log-evidence difference of 0.5 between successive iterations. To enhance the sampling efficiency and accuracy of the posterior distributions, we employed the random-walk sampling strategy alongside a multi-ellipsoidal bounding method. Two complementary stellar atmosphere model grids, PHOENIX (Husser et al. 2013) and Castelli-Kurucz (Castelli & Kurucz 2003), were utilized to reduce systematic dependencies associated with any single model set. For extinction correction, the Fitzpatrick (1999) reddening law was adopted, which provides reliable performance across optical and near-infrared bands. Each SED fit was computed using 100,000 posterior samples, enabling robust statistical characterisation of the model parameters.

For the SED fitting of individual cluster members, we adopted the geometric distance estimates provided by the Bayesian Bailer-Jones inference framework (Bailer-Jones et al. 2021), which are automatically retrieved and implemented by the ARIADNE SED-fitting tool (Vines & Jenkins 2022). These distances offer a significantly improved treatment of parallax uncertainties at ~ 2 kpc compared to direct inversion of parallaxes and therefore provide stable distance priors without fixing all stars to the same cluster value. Line-of-sight extinction values were taken from the Schlafly & Finkbeiner (2011) dust maps. Using these priors, the SED fitting constrains the key stellar parameters, effective temperature (T_{eff}), surface gravity ($\log g$), metallicity ([Fe/H]), interstellar extinction (A_V), and stellar radius (R), within a statistically consistent Bayesian framework appropriate for heterogeneous stellar populations in young OCs (Alzhrani et al. 2025; Bisht et al. 2026).

Astrometric reliability was assessed using the RUWE parameter, and stars with $\text{RUWE} > 1.4$ were excluded from the analysis. In addition to the RUWE criterion, we implemented two complementary filters from the *Gaia* DR3 database: the “variable” flag was used to discard sources with significant photometric variability that could compromise the stability of the SED fit, and the “duplicated source” flag was employed to eliminate entries affected by crowding or catalogue-level duplication. Following the application of these quality control measures, 259 stars were excluded from NGC 869 and 251 from NGC 884. Of the remaining stars, 349 in NGC 869 and 286 in NGC 884 were found to have a sufficient number of photometric measurements with reliable magnitudes to allow for the construction of robust SEDs. Consequently, the SED analyses were

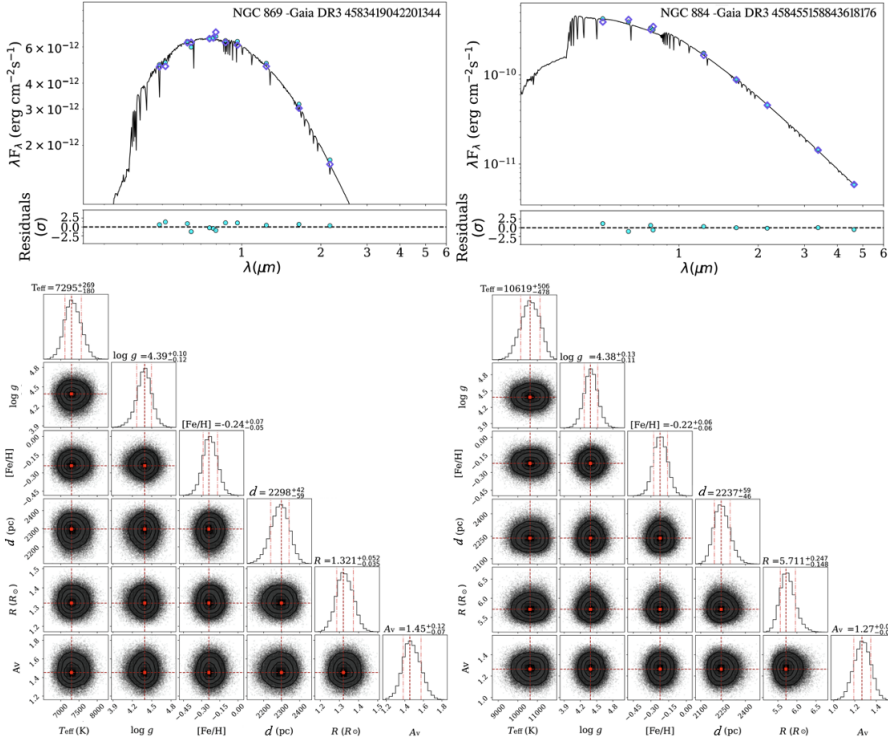


Fig. 10: The upper panels present the SED fits for representative selected one-member stars from each OC, while the bottom panels display the corresponding corner histograms and distributions of the best-fit astrophysical parameters.

limited to these subsets. As representative examples, one member star from each cluster was selected, and their corresponding SED fits together with the posterior distributions of the fitted parameters are shown in the form of SED distributions and corner plots in Figure 10.

The fundamental parameters derived from the SED analysis for the member stars of both OCs are presented in Table 3 and shown in Figure 11. As with many young OCs, the most significant sources of uncertainty are reddening and distance estimates. The colour excess ($E(B - V)$) values obtained from the SED analyses for the member stars of NGC 869 and NGC 884 were adapted to the *Gaia* photometric system using appropriate conversion coefficients. The resulting extinction, distance, and metallicity distributions exhibit narrow spreads, indicating a relatively homogeneous interstellar medium across both OCs. The mean extinction values are found to be $A_V = 1.50 \pm 0.10$ mag for NGC 869 and $A_V = 1.49 \pm 0.10$ mag for NGC 884, corresponding to colour excesses of $E(B - V) = 0.484 \pm 0.032$ mag and 0.481 ± 0.032 mag, respectively, assuming a standard total-to-selective extinction ratio of $R_V = 3.1$ (Cardelli et al. 1989). Both OCs exhibit slightly subsolar metallicities, with a mean value of $[Fe/H] = -0.25 \pm 0.03$ dex, corresponding to a metallicity fraction of $Z = 0.0088 \pm 0.0009$. The distance distributions are tightly clustered around mean values of 2378 ± 25 pc for NGC 869 and 2279 ± 31 pc for NGC 884. These fundamental parameters derived from the SED analysis are fully consistent, within uncertainties, with the values obtained from the MCMC-based isochrone fitting presented in Section 3.5. The agreement between these two independent approaches demonstrates the robustness of the adopted cluster parameters of both OCs.

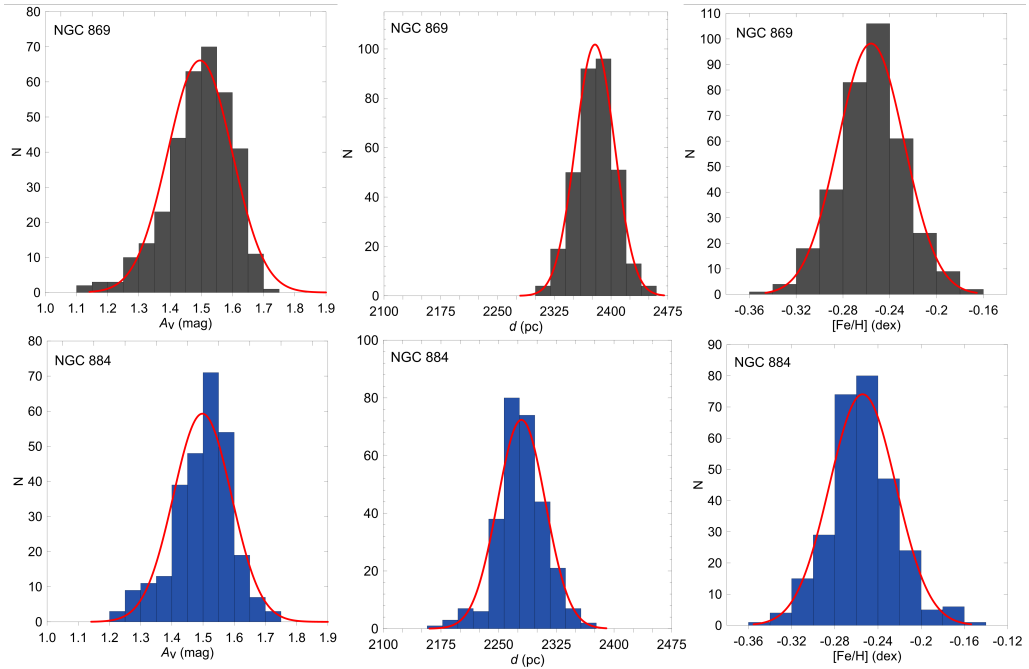


Fig. 11: Histograms illustrating the distributions of V -band extinction (A_V), and heliocentric distance (d) and metallicity ($[Fe/H]$) for stellar members of the NGC 869 and NGC 884, as derived from SED fitting. The red dashed lines correspond to standard Gaussian profiles.

4 KINEMATICAL AND DYNAMICAL ORBITAL ANALYSES

To estimate the Galactic orbital parameters of both OCs, we utilised the Python library `GALPY`³, which operates within the framework of the `MWPOTENTIAL2014` Galactic potential introduced by Bovy (2015). This potential represents the Milky Way as an axisymmetric system composed of three principal components: the bulge, the disc, and the halo. The bulge component follows a spherical power-law density profile as defined by Bovy (2015), the disc adopts the axisymmetric formulation described by Miyamoto & Nagai (1975), and the halo structure is modeled after the spherically symmetric dark-matter distribution proposed by Navarro et al. (1996). Detailed parameters used for orbital integrations and model fit within the `MWPOTENTIAL2014` framework are extensively documented in Bovy (2015). Based on their findings, we adopt Galactocentric distance of $R_0 = 8.125$ kpc (GRAVITY Collaboration et al. 2018), and a corresponding solar circular velocity of $V_\odot = 242$ km s $^{-1}$.

To explore the spatial distribution of the OCs within the MW, the Galactocentric distance (R_{gc}) was computed using the following formula (Tunçel Güçtekin et al. 2019):

$$R_{gc} = \sqrt{R_0^2 + (r \cos b)^2 - 2R_0 r \cos b \cos l}, \quad (6)$$

where R_0 is the distance from the Sun to the Galactic centre, r is the distance to OC, and l and b represent the Galactic longitude and latitude, respectively. The current distances of NGC 869 and NGC 884 from the Galactic centre are 9935 ± 237 and 9862 ± 215 pc, respectively.

Accurate determination of the space velocities and orbital properties of the OCs under study requires reliable estimates of their mean radial velocities. In this study, we did not restrict our analysis to radial

³ <https://galpy.readthedocs.io/en/v1.5.0/>

velocity measurements available solely in the *Gaia* DR3 catalogue (Gaia Collaboration et al. 2023). Instead, we extended our search by incorporating additional radial velocity measurements from the compilation of Tsantaki et al. (2022), which includes data from large spectroscopic surveys such as LAMOST and APOGEE. Candidate stars were identified by cross-matching the radial velocity catalogues with the OC membership lists and applying strict quality criteria. Specifically, only stars with membership probabilities $P \geq 0.7$ and reliable astrometric solutions characterized by $\text{RUWE} \leq 1.4$ were retained. For NGC 869, six stars were initially matched in the catalogue of Tsantaki et al. (2022). However, one star with a low membership probability ($P \approx 0.1$) and one star flagged as variable were excluded from the analysis. As a result, four stars from this catalogue were retained for NGC 869. For NGC 884, all stars matched in the same catalogue satisfied the membership probability and quality criteria, yielding a final sample of four non-*Gaia* stars. Consequently, a total of eight stars from external spectroscopic surveys (four in each OC) were included in addition to the *Gaia* DR3 radial velocity measurements.

In total, the final radial velocity samples comprise 13 stars for NGC 869 and 14 stars for NGC 884, with 9 and 10 stars, respectively, originating from the *Gaia* DR3 catalogue, and the remaining four stars in each OC taken from external spectroscopic surveys. Using the weighted mean method described by Carrera et al. (2022), we derived mean radial velocities of $V_R = -38.17 \pm 3.23 \text{ km s}^{-1}$ for NGC 869 and $V_R = -40.21 \pm 2.95 \text{ km s}^{-1}$ for NGC 884. The detailed stellar properties and survey origins are listed in Table 4, while the adopted mean values are listed in Table 3.

In comparing the mean radial velocity values obtained in this study, the current era of high-precision astrometric data provided by the *Gaia* mission has been considered. Soubiran et al. (2018), using *Gaia* DR2 data (Gaia Collaboration et al. 2018), reported a radial velocity of $V_R = -62.82 \pm 16 \text{ km s}^{-1}$ for NGC 869 based on a member star, and $V_R = -43.01 \pm 5.69 \text{ km s}^{-1}$ for NGC 884 based on two member stars. Similarly, Tarricq et al. (2021), also utilising *Gaia* DR2, derived a mean radial velocity of $V_R = -44.09 \pm 7.52 \text{ km s}^{-1}$ for NGC 869 from one member, and $V_R = -33.66 \pm 4.03 \text{ km s}^{-1}$ for NGC 884 from five members. More recently, Hunt & Reffert (2023), using *Gaia* DR3 data (Gaia Collaboration et al. 2023), calculated a mean radial velocity of $V_R = -67.64 \pm 10.42 \text{ km s}^{-1}$ for NGC 869 based on six member stars, and $V_R = -43.90 \pm 1.61 \text{ km s}^{-1}$ for NGC 884 based on two members. When considered in the context of these recent studies, the mean radial velocity for NGC 869 derived in the present work is consistent with the result reported by Tarricq et al. (2021), while the value obtained for NGC 884 shows strong agreement with both Soubiran et al. (2018) and Hunt & Reffert (2023). It should also be noted that the radial velocity estimates presented in this study are based on measurements from a total of 27 stars across both OCs.

4.1 Space Velocity Estimation

To estimate the mean space velocity components for both OCs we collected the equatorial coordinates (α, δ) of the OCs, as reported by Cantat-Gaudin et al. (2020), the mean proper-motion components $(\mu_\alpha \cos \delta, \mu_\delta)$ determined in Section 3.4, the MCMC-based distances (d_{iso}) from Section 3.5, and the radial velocities (V_R) estimated in this study (see Table 3). The space-velocity components of the NGC 869 and NGC 884 were computed using the `GALPY` package developed by Bovy (2015), and are listed Table 5). In this context, the U component denotes the velocity directed toward the Galactic centre, V represents

Table 4: Radial velocity data for stars with high membership probabilities in NGC 869 and NGC 884. The table lists the *Gaia* DR3 source IDs, equatorial coordinates, *G*-band magnitudes, radial velocities, RUWE values, membership probabilities, and the survey providing the radial velocity measurements.

Order	Gaia Source ID	α_{J2000} ($^{\circ}$)	δ_{J2000} ($^{\circ}$)	<i>G</i> (mag)	RV (km s^{-1})	RUWE	<i>P</i>	Survey*
NGC 869								
01	458357741598022528	35.1208	56.9931	6.65	-45.79 \pm 0.40	1.01	0.95	Gaia
02	458373035989882880	34.5629	57.1711	9.91	-8.51 \pm 13.06	1.00	0.90	Gaia
03	458373826264109312	34.9170	57.0920	9.86	-103.15 \pm 11.96	1.09	0.99	Gaia
04	458375235013296000	34.8081	57.1692	6.51	-43.56 \pm 1.72	0.98	0.97	Gaia
05	458379014584350592	34.6173	57.2084	8.11	-65.51 \pm 8.32	1.06	0.97	Gaia
06	458560159122834816	34.4875	57.1282	11.19	-100.39 \pm 29.55	1.01	0.99	Gaia
07	458561052475969920	34.4819	57.2188	12.33	-20.68 \pm 36.30	1.12	0.99	Gaia
08	458568164941730048	34.4304	57.3147	12.95	-62.16 \pm 4.81	1.05	0.77	Gaia
09	458569917288566528	34.7220	57.4213	7.40	-35.09 \pm 0.46	0.96	0.78	Gaia
10	458364652214200064	34.7035	56.8883	14.82	-13.32 \pm 2.81	0.97	0.95	LAMOST
11	458569401892222592	34.6447	57.3879	14.00	-0.62 \pm 2.68	1.01	0.88	LAMOST
12	458362487550472576	35.0999	57.0491	14.98	14.90 \pm 1.33	0.99	0.92	LAMOST
13	458374169861447296	34.9010	57.1203	15.72	-44.15 \pm 1.90	0.95	0.98	LAMOST
NGC 884								
01	458407464445792384	35.6012	57.1095	6.56	-46.18 \pm 0.37	1.06	0.99	Gaia
02	458414542551436672	35.7229	57.2452	7.22	-50.22 \pm 0.98	1.07	0.94	Gaia
03	458414989228047744	35.8505	57.2120	7.29	-45.69 \pm 0.14	1.02	0.95	Gaia
04	458454606008605312	35.5024	57.1450	7.97	-41.61 \pm 1.66	0.98	0.99	Gaia
05	458310604343959552	35.3395	56.8985	10.76	-86.96 \pm 15.42	1.31	0.87	Gaia
06	458413511759296896	35.8281	57.2162	10.98	-29.48 \pm 20.82	1.03	0.95	Gaia
07	458458454299129088	35.2199	57.2244	11.20	-47.05 \pm 3.02	1.10	0.98	Gaia
08	458452372625503744	35.3888	57.0324	11.38	-117.26 \pm 27.10	1.23	0.98	Gaia
09	458440071838143616	35.9335	57.3966	12.06	-44.35 \pm 23.43	1.22	0.84	Gaia
10	458461404928737024	35.6199	57.2662	12.33	-89.02 \pm 35.49	1.18	0.96	Gaia
11	458413339950196736	35.7963	57.1685	12.26	-3.72 \pm 0.35	0.98	0.94	APOGEE
12	458408937611303424	35.9408	57.0878	12.64	-9.91 \pm 3.06	1.17	0.73	LAMOST
13	458416879013598592	35.8433	57.3653	14.84	-24.10 \pm 2.77	1.01	0.94	LAMOST
14	458359670051882240	35.2682	57.0681	15.65	-18.51 \pm 1.68	1.06	0.98	LAMOST

(*): Survey denotes the source of the radial velocity measurements: *Gaia* (Gaia DR3), LAMOST (Large Sky Area Multi-Object Fibre Spectroscopic Telescope), and APOGEE (Apache Point Observatory Galactic Evolution Experiment).

the velocity in the direction of Galactic rotation, and W indicates the velocity component perpendicular to the Galactic plane, pointing toward the north Galactic pole (Bilir et al. 2012; Döner et al. 2023). The uncertainties associated with the space-velocity components were quantified following the method proposed by Johnson & Soderblom (1987). To account for the motion relative to the local standard of rest (LSR), we adopted the correction values of $(8.83 \pm 0.24, 14.19 \pm 0.34, 6.57 \pm 0.21) \text{ km s}^{-1}$, as reported by Coşkunoğlu et al. (2011). After applying these corrections, the LSR-adjusted velocity components were recalculated as: $(U, V, W)_{\text{LSR}} = (39.63 \pm 1.88, -13.13 \pm 2.20, -5.47 \pm 1.63) \text{ km s}^{-1}$ for NGC 869 and $(37.73 \pm 2.20, -12.02 \pm 2.29, -5.08 \pm 1.41) \text{ km s}^{-1}$ for NGC 884. In addition, the total space velocity (S_{LSR}) to the LSR for each OC was derived from their respective mean total space velocity components (Coşkunoğlu et al. 2012).

$$S_{\text{LSR}} = \sqrt{U_{\text{LSR}}^2 + V_{\text{LSR}}^2 + W_{\text{LSR}}^2}. \quad (7)$$

Table 5: The spatial, kinematic, Galactic orbital, and dynamical parameters of both OCs are presented.

Parameter	NGC 869	NGC 884
Spatial Parameters		
X_\odot (pc)	-1666 \pm 203	-1606 \pm 186
Y_\odot (pc)	1687 \pm 206	1603 \pm 186
Z_\odot (pc)	-155 \pm 19	-141 \pm 17
R_{gc} (pc)	9935 \pm 237	9862 \pm 215
Kinematical Parameters		
\bar{U} (km s $^{-1}$)	30.79 \pm 1.86	28.90 \pm 2.19
\bar{V} (km s $^{-1}$)	-27.32 \pm 2.17	-26.21 \pm 2.27
\bar{W} (km s $^{-1}$)	-12.04 \pm 1.61	-11.65 \pm 1.390
U_{LSR} (km s $^{-1}$)	39.63 \pm 1.88	37.73 \pm 2.20
V_{LSR} (km s $^{-1}$)	-13.13 \pm 2.20	-12.02 \pm 2.29
W_{LSR} (km s $^{-1}$)	-5.47 \pm 1.63	-5.08 \pm 1.41
S_{LSR} (km s $^{-1}$)	42.11 \pm 3.31	39.92 \pm 3.47
\bar{V}_x (km s $^{-1}$)	-4.15 \pm 0.50	-3.65 \pm 0.52
\bar{V}_y (km s $^{-1}$)	-12.44 \pm 3.53	-11.25 \pm 3.35
\bar{V}_z (km s $^{-1}$)	-41.10 \pm 6.41	-39.29 \pm 6.27
A_o (o)	-108.43 \pm 0.09	-107.96 \pm 0.09
D_o (o)	-72.30 \pm 0.12	-73.24 \pm 0.12
Galactic Orbital Parameters		
R_a (pc)	9949 \pm 209	9926 \pm 216
R_p (pc)	9384 \pm 473	9444 \pm 428
R_m (pc)	9667 \pm 341	9685 \pm 322
Z_{max} (pc)	154 \pm 31	143 \pm 27
e	0.029 \pm 0.015	0.025 \pm 0.012
P_{orb} (Myr)	250 \pm 10	251 \pm 9
R_{birth} (pc)	9876 \pm 148	9841 \pm 126
Dynamical Parameters		
T_{relax} (Myr)	29	40
r_t (pc)	2.04	3.26
τ_{ev} (Myr)	4000	5200

Based on these values, the total space velocities relative to the LSR were derived as $S_{\text{LSR}} = 42.11 \pm 3.31$ km s $^{-1}$ for NGC 869 and $S_{\text{LSR}} = 39.92 \pm 3.47$ km s $^{-1}$ for NGC 884. These results are indicative of kinematic properties typical for young thin-disc stellar populations, as discussed by Leggett (1992); Yontan et al. (2023).

Soubiran et al. (2018) investigated the kinematic properties of the NGC 869 and NGC 884 using astrometric data from *Gaia* DR2 (Gaia Collaboration et al. 2018), reporting space velocity components of $(U, V, W) = (46.96 \pm 11.29, -43.00 \pm 11.44, -9.71 \pm 1.05)$ km s $^{-1}$ for NGC 869 and $(32.72 \pm 4.02, -29.17 \pm 4.01, -10.81 \pm 0.37)$ km s $^{-1}$ for NGC 884. The findings of the present study reveal a notable divergence from the results of Soubiran et al. (2018) for NGC 869, while demonstrating a high level of agreement for NGC 884. The inconsistency in the case of NGC 869 is most likely due to the methodological constraint in Soubiran et al. (2018), wherein the cluster's radial velocity was estimated using data from one member star. Such a limited sample may not reliably represent the systemic motion of the cluster, thereby introducing potential biases into the derived space velocity components.

The member stars of OCs typically demonstrate coherent proper-motion vectors that, when extended across the celestial sphere, appear to converge toward a specific region termed the convergent point (CP). This geometrical behavior arises from the shared kinematic motion of OC members through space and

offers valuable constraints on the systemic dynamics of the cluster (Elsanhouri et al. 2018; Elsanhoury et al. 2025b). Estimation of CP coordinates enables researchers to probe the internal kinematic alignment and the dynamical cohesion of the cluster system.

To estimate the CP coordinates for both OCs, we employed the apex-declination diagram (AD-diagram) technique proposed by Chupina et al. (2001); Chupina et al. (2006), a method widely used for stellar systems exhibiting group motion. This approach involves mapping the velocity vector-derived apex coordinates (A_o , D_o), where A_o and D_o indicate the right ascension and declination of the CP, respectively. The intersection region of these vectors for cluster members marks the inferred CP position. In this study, we adopted the analytical framework formulated by Haroon et al. (2025), which relates the CP coordinates to the mean space velocity components (\bar{V}_x , \bar{V}_y , \bar{V}_z) by trigonometric transformations as follows (see Table 5). For each star, the components of the space velocity vector were computed within a right-handed rectangular coordinate system defined with respect to the equatorial reference frame, ensuring consistency with standard astrometric conventions.

$$\begin{aligned} V_x &= -V_\alpha \sin \alpha - (V_\delta \sin \delta - V_R \cos \delta) \cos \alpha, \\ V_y &= V_\alpha \cos \alpha - (V_\delta \sin \delta - V_R \cos \delta) \sin \alpha, \\ V_z &= V_\delta \cos \delta + V_R \sin \delta. \end{aligned} \quad (8)$$

Here, α and δ are the equatorial coordinates of the cluster member stars, V_R is the mean radial velocity of the OCs, and V_α and V_δ denote the components of the total space velocity corresponding to the proper motion in the right ascension ($\mu_\alpha \cos \delta$) and declination (μ_δ), respectively, and are defined by the following relations.

$$V_\alpha = 4.74047 \times d_{\text{iso}} \times \mu_\alpha \cos \delta, \quad V_\delta = 4.74047 \times d_{\text{iso}} \times \mu_\delta, \quad (9)$$

where d_{iso} is the distance of the cluster calculated by the isochrone fitting method (see Table 5). The resulting apex positions for NGC 869 and NGC 884 are depicted as crosses in Figure 12 with applied the AD-diagram method described in some studies in the literature (e.g. Elsanhoury 2016; Elsanhoury & Amin 2019; Elsanhoury 2025; Elsanhoury et al. 2025a). Each stellar apex represents the point on the celestial sphere where the spatial velocity vector intersects. The cluster apex coordinates (A_o , D_o) are computed using:

$$A_o = \tan^{-1} \left(\frac{\bar{V}_y}{\bar{V}_x} \right), \quad (10)$$

$$D_o = \tan^{-1} \left(\frac{\bar{V}_z}{\sqrt{\bar{V}_x^2 + \bar{V}_y^2}} \right). \quad (11)$$

Here, following the averaging of the velocity components \bar{V}_x , \bar{V}_y , and \bar{V}_z , the equatorial coordinates of the CP were subsequently determined and listed in Table 5, and these coordinates were shown in Figure 12.

4.2 Galactic Orbital Parameters

To derive the orbital characteristics of both OCs, we used the MWPOTENTIAL2014 Galactic potential model. The input parameters included the equatorial coordinates (α , δ), the mean proper-motion components ($\mu_\alpha \cos \delta$, μ_δ), the distances (d_{iso}), and the radial velocities (V_R) as listed in Table 3. To ensure sufficient

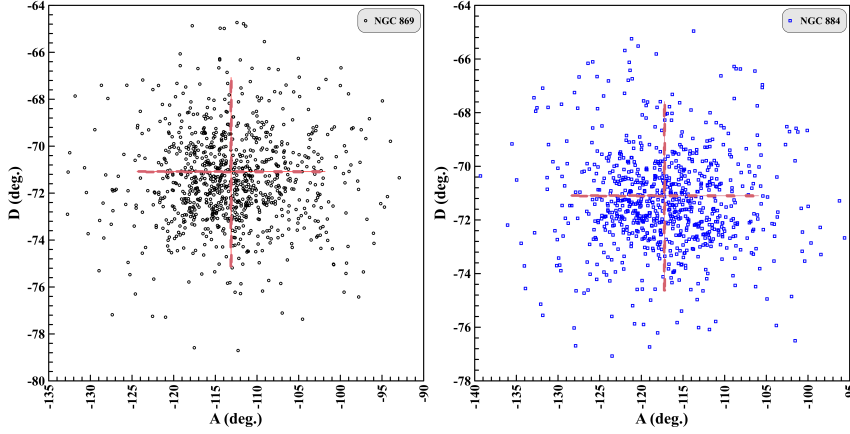


Fig. 12: CP diagrams illustrating the apex solutions (A_o, D_o) for NGC 869 and NGC 884; the apex coordinates are marked by a cross symbol.

temporal resolution for determining the minimum separation, orbital integration was performed backward in time using a time step of 0.1 Myr over a total timespan of 2 Gyr. This duration was chosen to ensure complete orbital closure and to obtain robust estimates of the Galactic orbital parameters. The resulting parameters are also presented in Table 5, where R_a and R_p correspond to the apogalactic and perigalactic distances, respectively. The orbital eccentricity is denoted by e , while Z_{\max} indicates the maximum vertical distance from the Galactic plane.

While the 3D orbits of the investigated OCs around the Galactic centre, computed using `GALPY`, are presented in the upper panels of Figure 13, the lower panels show the Galactic orbital trajectories of NGC 884 and NGC 869, projected onto the $Z \times R_{\text{gc}}$ planes. As can be seen from Figure 13, neither OC deviates significantly from the Galactic plane and follows a similar orbit with a comparable eccentricity around the Galactic centre. As summarised in Table 5, the orbital analysis shows that NGC 869 and NGC 884 follow low-eccentricity, nearly circular orbits near 9–10 kpc, with small vertical excursions ($Z_{\max} \sim 140$ –160 pc) that keep them within the Galactic thin disk. Their similar orbital periods and radial motions further indicate that both clusters share comparable dynamical histories, consistent with formation in a common large-scale Galactic environment. The low eccentricities of both OCs and small deviations from the Galactic plane suggest that NGC 869 and NGC 884 are dynamically associated with the thin-disc component of the MW (Taşdemir & Yontan 2023; Canbay et al. 2025; Çınar et al. 2024, 2025).

To examine whether the two investigated OCs originated from nearby regions of the Galaxy, their present-day positions within the Galaxy were plotted on the $R_{\text{gc}} \times t$ plane, and their birthplaces were investigated by tracing their orbits backward in time over a period corresponding to their estimated ages (Yücel et al. 2024; Taşdemir et al. 2025). In Figure 14, the present-day positions of the OCs are indicated by yellow circles, and their estimated birthplaces are marked with triangles, while the shaded regions and dotted lines represent the orbital uncertainties arising from the propagation of errors in the astrometric (proper motions and distances) and spectroscopic (radial velocities) input parameters. Backward orbital integrations under a static Galactic potential were used to estimate the likely birth radii of NGC 869 and NGC 884. This classical traceback approach (Akbaba et al. 2024) provides a simple means of assessing whether the clusters have experienced significant radial migration. Our calculations indicate that both OCs were probably

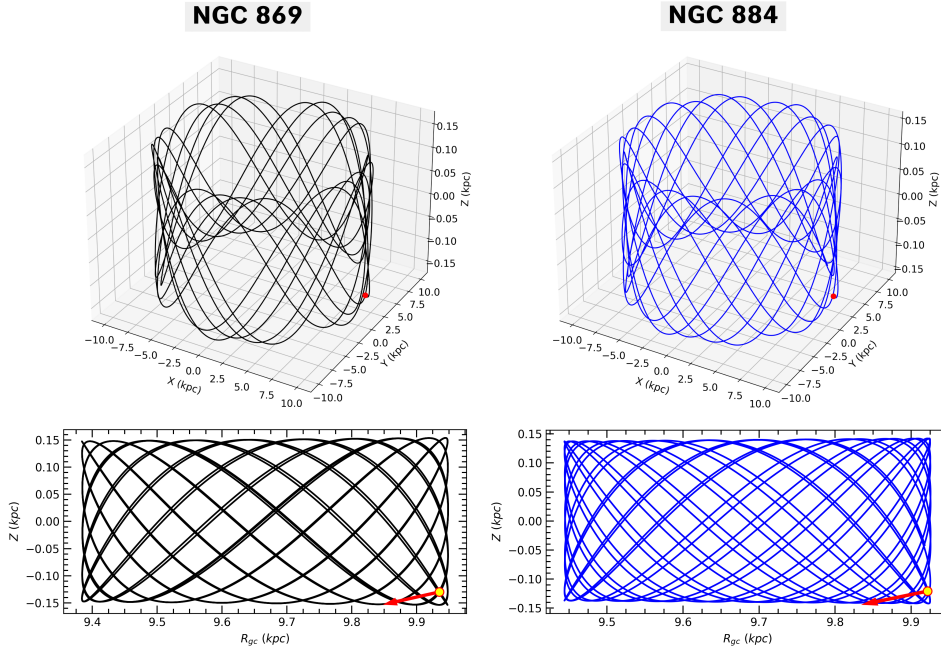


Fig. 13: The 3D orbits of the OCs around the Galactic centre are shown. In the upper panels, red dashed circles mark the present-day positions of the OCs, while the lower panels display the Galactic orbits of NGC 869 and NGC 884 projected onto the $Z \times R_{\text{gc}}$ planes. The red arrow indicates the direction of motion for both OCs.

formed at Galactocentric distances very close to their current locations, with inferred birthplace radii of $R_{\text{birth}} = 9876 \pm 148$ and 9841 ± 126 pc, respectively.

The similarity in their orbital parameters, along with their proximity in both position and age, further supports the scenario of a common origin. The results of the dynamical orbital integration are consistent with the hypothesis that NGC 884 and NGC 869 formed in nearby regions of the Galactic disc and have subsequently evolved as a co-moving cluster pair. Such consistency between past orbital properties and future orbital convergence strengthens the interpretation that these clusters not only share a common origin but may also experience renewed dynamical interaction. Figure 14b displays orbital integration of NGC 869 and NGC 884, indicating that, although the two OCs do not currently exhibit strong signs of mutual gravitational binding, their orbits will bring them significantly closer in the future. Specifically, at $t \approx 11$ Myr, the pair reaches its absolute closest approach with a minimum 3D intercluster separation of $\Delta_{3D} \approx 26$ pc. This projected proximity, which is comparable to the sum of their tidal radii, suggests a grazing encounter that may lead to transient dynamical interactions or even a brief bound phase, highlighting the importance of considering future orbital evolution in the study of potential BOCs.

Although our results show that NGC 869 and NGC 884 are currently not gravitationally bound, as their present-day separation (103 pc) significantly exceeds the sum of their tidal radii (~ 26 pc), the forward integration of their orbits reveals a particularly intriguing outcome. After approximately 11 Myr, the 3D separation between the two OCs decreases to 26 pc, and is shown in Figure 14c. This future convergence suggests a potential close encounter or even a dynamical interaction event between the two OCs. Unlike the ongoing collision scenario of two unrelated clusters reported by Piatti & Malhan (2022), where IC 4665 and

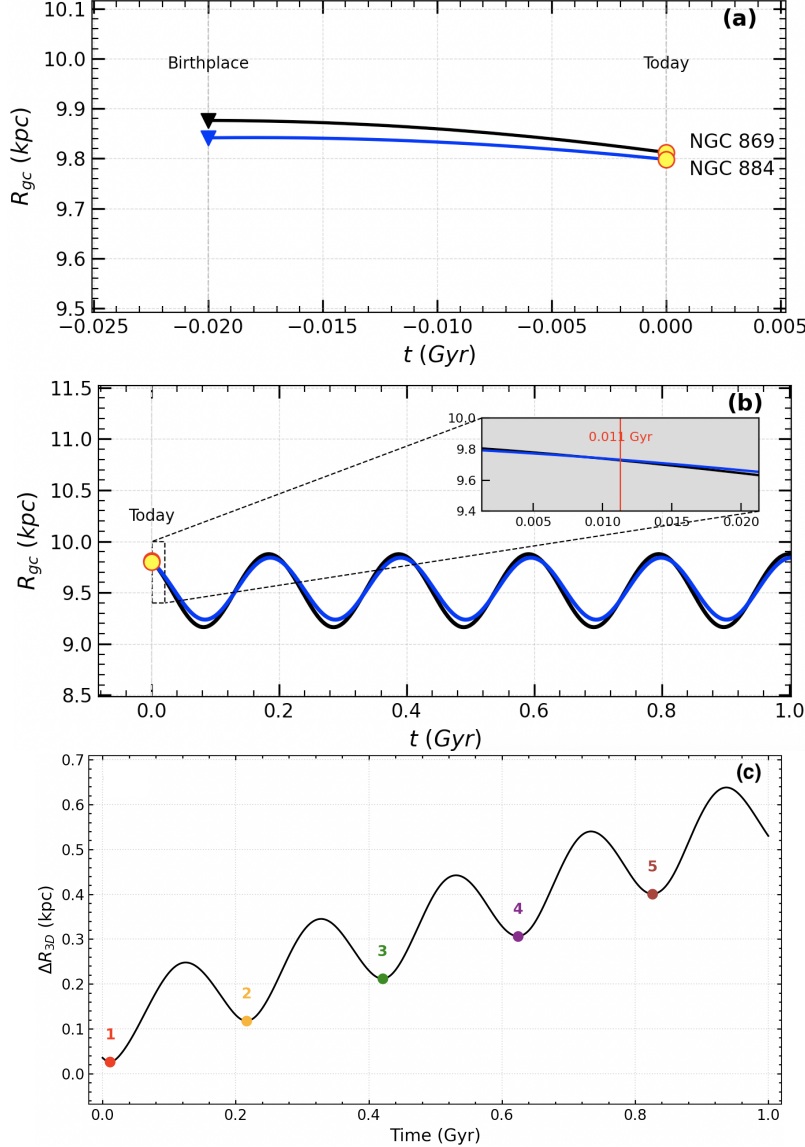


Fig. 14: The orbital dynamics and separation history of NGC 869 (black line) and NGC 884 (black line). Panel (a) displays the orbital tracebacks over the past ~ 20 Myr in the $R_{gc} \times t$ plane, highlighting the estimated birthplace. Filled yellow circles indicate present-day positions ($t = 0$), while triangles mark the inferred birthplaces. Panel (b) illustrates the future orbital evolution of both OCs over the next 1 Gyr. The inset provides a zoomed-in view of the pair's closest spatial encounter, which occurred at $t \approx 11$ Myr. Panel (c) shows the temporal evolution of the 3D separation (ΔR_{3D}) between the two clusters. The numbered colored circles (1–5) correspond to the epochs of local minima (closest approaches) in their mutual distance.

Collinder 350 first come into contact at the present epoch after forming independently, our system illustrates the inverse case, a pair of clusters that may experience significant mutual interaction in the future, despite not being currently bound. Such predictions highlight the dynamical richness of binary or near-BOCs and raise the possibility that gravitationally unbound cluster pairs can still engage in tidal encounters over long time-scales, depending on their relative orbital configurations within the Galactic potential.

5 DYNAMICAL PARAMETERS AND MASS DISTRIBUTION

5.1 Luminosity Function

The stellar content of the BOC system NGC 869 and NGC 884 was further analyzed through the construction of luminosity and present-day mass functions (PDMFs) based on high-precision astrometric and photometric data from the *Gaia* DR3 release. The luminosity function (LF) characterises the distribution of stars over intervals of absolute G -band absolute magnitudes (M_G). For this purpose, stars with reliable photometric and astrometric measurements were selected, and the LFs were computed in bins of 1 mag, which primarily trace the MS population. Figure 15 displays the resulting LFs, indicating a relative incompleteness toward the faint end due to photometric limitations, particularly fainter than $G \sim 20.5$ mag. This observational bias impacts the detection of low-mass members and slightly alters the slope at the faint tail of the LF. The observed variations in the luminosity function, when considered together with previously reported radial trends in the $h-\chi$ Persei system, are consistent with mass segregation, wherein more massive stars are preferentially concentrated toward the cluster centers (e.g., Slesnick et al. 2002a; Sharma et al. 2008; Hasan & Hasan 2011).

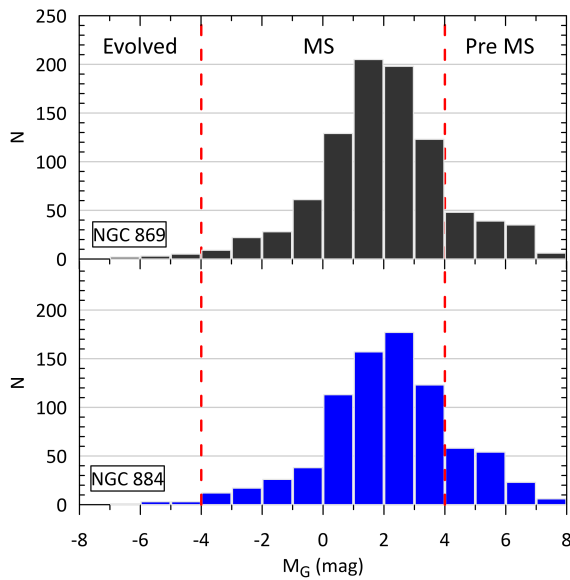


Fig. 15: LFs of cluster member stars belonging to different luminosity classes in NGC 869 (upper panel) and NGC 884 (lower panel).

5.2 Present Day Mass Function

To calculate the PDMFs of each OC, we adopted a standard power-law form of the initial mass function (IMF) expressed as follows:

$$\log \left(\frac{dN}{dM} \right) = -(1 + \Gamma) \times \log(M) + \text{constant} \quad (12)$$

where dN/dM represents the number of stars per unit mass interval and Γ is the slope of the function. For stars with masses greater than $1 M_\odot$, this formalism is consistent with the classical Salpeter IMF, which assumes $\Gamma = 1.35$ (Salpeter 1955). Masses of the main-sequence stars were estimated using a fourth-order

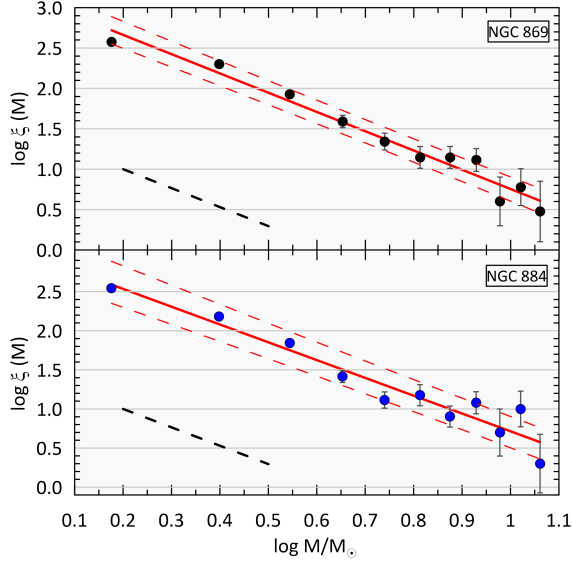


Fig. 16: PDMF of NGC 869 (upper panel) and NGC 884 (lower panel). Red lines represent the PDMFs of both OCs, while red dashed lines are the $\pm 1\sigma$ standard deviations. The black dashed lines in the panels represent the slope of Salpeter (1955).

polynomial relation between M_G and M/M_\odot , calibrated using PARSEC isochrones by Bressan et al. (2012), as follows:

$$\left[\frac{M}{M_\odot} \right] = 3.95592 - 1.57215 M_G + 0.25287 M_G^2 + 0.01953 M_G^3 - 0.00753 M_G^4. \quad (13)$$

Using this mass-luminosity relation (MLR), the masses of individual member stars were computed, and the resulting mass distributions were used to build the PDMFs of both OCs. Figure 16 shows the derived PDMFs, along with their best-fit slopes. For NGC 869, the slope is $\Gamma = 1.12 \pm 0.06$, and for NGC 884, it is $\Gamma = 1.17 \pm 0.06$. Both values are in close agreement with the canonical Salpeter (1955) slope as $\Gamma = 1.35$, suggesting that the stellar populations of the clusters follow a standard IMF for the mass range analysed. The relatively steep slopes also indicate an excess of low-mass stars compared to high-mass stars, as expected for young OCs.

In the analysis of the mass distributions of both OCs investigated in this study, the luminosity classes of the cluster members were considered. The luminosity classes of the member stars were determined using the CMDs of the OCs, and the number of stars in these groups, their total masses, and mean masses were calculated and listed in Table 6. As a result of the analysis, the total masses of NGC 869 and NGC 884 were calculated as $2119 M/M_\odot$ and $1800 M/M_\odot$, respectively. These findings indicate that NGC 869 is more massive than NGC 884.

5.3 The Dynamical State of Mass Segregation

The dynamical relaxation time (T_{relax}) provides a crucial measure of the time required for a stellar system to approach a state of kinetic equilibrium, where energy redistribution among member stars leads to the

Table 6: Stellar mass distribution of NGC 869 and NGC 884 subdivided by luminosity class (LC): evolved stars, main sequence (MS), and pre-main sequence (Pre-MS) members. N is the number of stars in the luminosity class; $\sum M$ and $\langle M \rangle$ represent the total and mean masses, respectively, in solar masses.

LC	NGC 869		
	N	$\sum M(M_\odot)$	$\langle M \rangle(M_\odot)$
Evolved	9	103	11.44
MS	718	1940	2.70
Pre-MS	81	76	0.94
Total	808	2119	2.62
LC	NGC 884		
	N	$\sum M(M_\odot)$	$\langle M \rangle(M_\odot)$
Evolved	7	80	11.43
MS	606	1630	2.69
Pre-MS	94	90	0.96
Total	707	1800	2.55

stabilisation of internal motions. In the context of OCs such as NGC 869 and NGC 884, this timescale serves as a key diagnostic for assessing the level of internal dynamical evolution. A relatively short T_{relax} implies that the system has undergone considerable internal interactions such as two-body encounters and mass segregation, leading toward dynamical maturity. Conversely, a long relaxation time suggests that the cluster remains dynamically young and may still retain features reflecting its initial conditions.

To estimate T_{relax} for both OCs, we adopt the formalism introduced by Spitzer & Hart (1971), given as:

$$T_{\text{relax}} = \frac{8.9 \times 10^5 N^{1/2} R_h^{3/2}}{\langle M_C \rangle^{1/2} \log(0.4N)}, \quad (14)$$

where N represents the total number of cluster members, $\langle M_C \rangle$ is the mean stellar mass in Solar units, and R_h is the half-mass radius in parsecs. To derive R_h , we apply the semi-empirical relation provided by Šablevičiūtė et al. (2006):

$$R_h = 0.547 \times r_c \times \left(\frac{r_t}{r_c} \right)^{0.486}, \quad (15)$$

in which r_c and r_t correspond to the core and tidal radii, respectively. As mentioned in Section 3.2, the r_t parameter in the relation has been adopted as r_{lim} . In this study, instead of estimating the tidal radius using an analytical expression, the values listed in Table 2 were adopted. The core radii of NGC 869 and NGC 884 are obtained from the fitted RDPs, and using these parameters, we calculate the half-mass radii to be approximately 2.76 ± 0.05 pc for NGC 869 and 3.54 ± 0.05 pc for NGC 884. Substituting these values into Equation 14, we derive the relaxation times as $T_{\text{relax}} \approx 29$ Myr for NGC 869 and 40 Myr for NGC 884. Since both OCs have ages of about 20 Myr, they have not yet completed a full relaxation cycle. Nevertheless, the presence of early mass segregation, common in dynamically young OCs, may reflect rapid internal evolution driven by their initial density structure or by primordial mass segregation, rather than long-term two-body relaxation.

Based on the MCMC-based distance estimates, the current separation between NGC 869 and NGC 884 is approximately 103 pc. The tidal radii of both OCs are calculated as 13.24 pc and 12.90 pc, respectively, yielding a total tidal extent of 26.14 pc. The ratio of their spatial separation to the combined tidal radius is

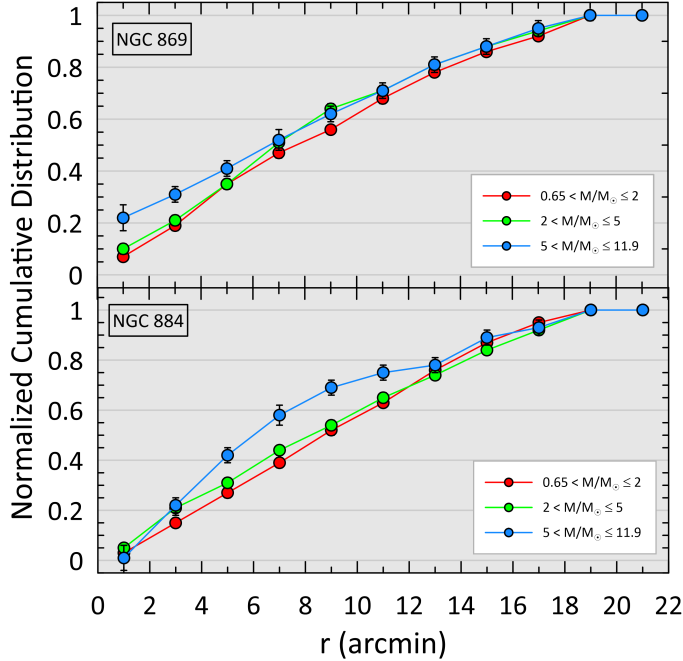


Fig. 17: Cumulative radial distributions of stars stratified by mass for NGC 869 (upper panel) and NGC 884 (lower panel).

therefore:

$$\frac{d_{\text{separation}}}{r_{\text{tidal, total}}} = \frac{103}{26.14} \approx 3.94. \quad (16)$$

Since this ratio significantly exceeds unity, it indicates that both OCs lie quite beyond the tidal influence of each other. Consequently, we conclude that NGC 869 and NGC 884 are currently not gravitationally bound. Despite their close spatial proximity and similar ages, the current separation implies that they are a coeval but unbound OC pair, likely originating from a common star-forming region but no longer dynamically coupled.

The long-term dynamical evolution of OCs is significantly influenced by internal gravitational interactions among member stars, which lead to the gradual redistribution of energy and the eventual loss of members. One of the key timescales characterizing this process is the evaporation time (τ_{ev}), which represents the time required for the cluster to lose the majority of its stars due to internal relaxation mechanisms (Adams & Myers 2001). For clusters in a state of virial equilibrium, the evaporation time is approximately $\tau_{\text{ev}} \sim 100 \times T_{\text{relax}}$, where T_{relax} is the dynamical relaxation time. For the clusters studied here, this relation yields $\tau_{\text{ev}} \approx 2000$ Myr, substantially longer than the canonical 100 Myr value cited for classical OCs. This demonstrates that their full dynamical dissolution proceeds on multi-Gyr timescales. To evaluate the current dynamical state of the clusters, we computed the dynamical evolution parameter $\tau = \text{age}/T_{\text{relax}}$, a dimensionless indicator of dynamical maturity, where systems with $\tau \gg 1$ are dynamically evolved or relaxed, and those with $\tau \ll 1$ are dynamically young and still relaxing. For NGC 869 and NGC 884, the derived τ values show that both OCs have advanced substantially in their dynamical evolution, indicating partial relaxation despite their relatively young ages.

To examine mass segregation in the BOCs, cluster members were divided into three equal-number mass bins: high-mass ($5 < M/M_{\odot} \leq 11.9$), intermediate-mass ($2 < M/M_{\odot} \leq 5$), and low-mass ($0.65 < M/M_{\odot} \leq 2$) stars. The normalised cumulative radial distributions (Figure 17) reveal a clear mass segregation

signature in both OCs, with high-mass stars preferentially concentrated toward the cluster cores, likely due to dynamical relaxation, while intermediate- and low-mass stars exhibit more extended radial distributions toward the outskirts. The results reveal a clear signature of mass segregation, manifested by the enhanced central concentration of high-mass stars relative to their lower-mass counterparts. Such a distribution is commonly interpreted as a consequence of dynamical relaxation, where two-body interactions drive more massive stars toward the cluster core over time. In contrast, intermediate- and low-mass stars exhibit broader radial distributions, preferentially populating the outer regions of the clusters. However, given the young ages of NGC 869 and NGC 884, the observed degree of mass segregation may not be fully explained by dynamical evolution alone. An alternative or complementary explanation is the presence of primordial mass segregation, whereby massive stars form preferentially in the densest central regions during the early stages of cluster formation (Bonnel et al. 1998; Hillenbrand & Hartmann 1998; Allison et al. 2009). Several theoretical and observational studies have shown that massive stars can be centrally concentrated at birth, particularly in clusters formed within dense molecular environments, without requiring significant dynamical evolution (McMillan et al. 2007; Parker et al. 2016). Therefore, the mass segregation observed in the h and χ Persei system is likely the result of a combination of early formation conditions and subsequent dynamical relaxation, consistent with their interpretation as co-evolved BOCs.

To quantitatively evaluate the degree of mass segregation, the Kolmogorov-Smirnov (K-S) statistical test was applied in a pairwise manner to compare the cumulative radial distributions of high-mass stars with those of intermediate- and low-mass stellar populations separately. For NGC 869, the comparison between high-mass and intermediate-mass stars resulted in a p -value of 0.005, while the comparison between high-mass and low-mass stars yielded a p -value of 0.007. Similarly, for NGC 884, the corresponding p -values were 0.003 and 0.009, respectively. In all cases, the obtained p -values are below 0.01, allowing us to reject the null hypothesis that the compared stellar populations are drawn from the same parent distribution. These statistically significant differences indicate that high-mass stars exhibit a spatial distribution distinct from that of lower-mass stars, providing strong evidence for the presence of mass segregation in both OCs under study.

6 DISCUSSION

We have conducted a comprehensive investigation of the structural, astrometric, photometric, kinematical, and dynamical characteristics of the BOCs NGC 869 and NGC 884 using *Gaia* DR3 data. Our findings reinforce the well-established binary nature of these prominent BOCs, commonly known as h and χ Persei (Currie et al. 2010). While their physical association has been widely acknowledged in the literature, a unified and multi-dimensional analysis encompassing all major cluster properties has been lacking. This study fills that gap by presenting an integrated approach that brings together multiple lines of evidence, offering a more complete understanding of their formation history and dynamical state.

Despite the lack of spectroscopic data for both OCs, the agreement between the mean values calculated from the distributions of the parameters obtained by the MCMC and SED methods revealed that the fundamental parameters for both OCs were determined with high accuracy and precision. The fundamental parameters (T_{eff} , $\log g$, $[\text{Fe}/\text{H}]$, Av and d) were determined from the SED analyses of total 635 member stars in both OCs, and the histograms of the parameters were plotted and their mean values were calculated by fitting Gaussian

curves. Both OCs exhibit slightly metal-poor metallicities of $[\text{Fe}/\text{H}] = -0.25 \pm 0.03$ dex and consistent mean V -band extinctions of $A_V \approx 1.5$ mag, corresponding to colour excess values of $E(B-V) \approx 0.48$ mag. The distance distributions are around 2300 pc, consistent with previous results based on isochrone fitting and *Gaia* trigonometric parallaxes (e.g., Currie et al. 2010; Cantat-Gaudin et al. 2018b).

A critical challenge in SED-based stellar characterisation lies in the intrinsic parameter degeneracies, most notably among effective temperature, V -band extinction, and stellar radius, that can bias the physical modeling (McDonald et al. 2017). To address this, we applied a multi-faceted approach aimed at reducing degeneracy and driven uncertainty. Our method incorporated high-precision *Gaia* DR3 trigonometric parallaxes, extinction priors from 3D Galactic dust maps (Schlafly & Finkbeiner 2011), and Bayesian model averaging across two independent stellar atmosphere model grids (PHOENIX and Castelli-Kurucz). Additionally, the use of nested sampling with high posterior resolution allowed for better exploration of the multi-dimensional parameter space. These efforts yielded robust parameter estimates for both OCs with minimal scatter. The reduction of model-dependent biases supports our conclusion that these clusters form a physically bound system (Bragg & Kenyon 2005). Moreover, these consistent parameter values suggest that both OCs formed under very similar interstellar conditions within the Galactic disc (Fujimoto & Kumai 1997; Fellhauer & Kroupa 2005).

Dynamical orbit integration using high-precision astrometric data from *Gaia* DR3 reveals that both OCs exhibit remarkably similar Galactic trajectories and nearly indistinguishable birthplaces, providing strong kinematic support for their coeval formation. The orbital paths traced over the past about $t = 20$ Myr show minimal divergence in space velocities and proper-motion components within the Galactic disc, effectively ruling out scenarios of gravitational capture or chance alignment. Instead, the results support a primordial BOC origin, in which both OCs were born simultaneously in closely related regions of the Galactic disc. Furthermore, both OCs are currently not gravitationally bound due to their large separation relative to their tidal radii, orbital integration predicts a close approach in ≈ 11 Myr. At that time, the two systems are expected to experience a closest approach of approximately 26 pc, which may indicate a future dynamical interaction. This contrasts with scenarios where clusters collide after independent formation, highlighting instead a case where initially unbound OCs may engage in significant tidal encounters over time. These results underline the complex dynamical evolution of binary or near-BOCs and the potential for gravitational interactions long after their formation (Piatti & Malhan 2022).

Both OCs exhibit similar total stellar masses, estimated as $2119 M_\odot$ for NGC 869 and $1800 M_\odot$ for NGC 884. The slopes of their PDMFs also show a close match, with $\Gamma = 1.12 \pm 0.06$ and 1.17 ± 0.06 , respectively, closely aligning with the canonical Salpeter value. Using the isochrone fitting method, BOC ages are obtained as $\log(t/\text{yr}) \cong 7.30 \pm 0.15$ for both OCs. The same age estimates, combined with the detection of mild mass segregation in both OCs cores, suggest a shared dynamical evolution (Horie et al. 2024). Taken together, these findings support a scenario in which NGC 869 and NGC 884 formed nearly simultaneously in closely related regions of the Perseus arm. The formation could have been triggered by large-scale processes such as a supernova shock wave (Boss & Keiser 2012; Iffrig & Hennebelle 2015) or a cloud-cloud collision (Horie et al. 2024), both of which are consistent with models of BOC formation in dense stellar environments (Slesnick et al. 2002b).

The CMDs of both OCs exhibit well-defined and nearly identical main-sequence and pre-main-sequence stellar populations (Slesnick et al. 2002b). The MCMC-based isochrone fitting and SED analyses used to determine the fundamental parameters yield consistent metallicity and extinction estimates. The alignment of the evolutionary sequences in both OCs further suggests that NGC 869 and NGC 884 formed within closely related regions of the Perseus spiral arm (Reid et al. 2019; Currie et al. 2010). Taken together, these multi-dimensional diagnostics indicate that both OCs are not only spatially and kinematically associated, but also share a common evolutionary history. The combined photometric, kinematic, and orbital evidence supports the interpretation of NGC 869 and NGC 884 as primordial BOCs within the Perseus arm. Nevertheless, uncertainties remain regarding their interaction with the surrounding OB association (Per OB1), and future multi-wavelength and spectroscopic studies will be essential to better constrain the environmental effects that may have influenced their subsequent evolution (Cappa et al. 1996).

Ultimately, the binary nature of NGC 869 and NGC 884 offers a unique laboratory for studying the early dynamical evolution of massive clusters, the impact of the Galactic tidal field, and the mechanisms by which bound cluster pairs survive over tens of millions of years. Continued high-precision astrometry, combined with advanced stellar population modeling and N-body simulations, will be essential to fully clarify the formation pathways and dynamical lifetimes of such BOCs. Future high-precision astrometric and spectroscopic studies could provide tighter constraints on age spreads, binarity, and internal dynamics, offering deeper insight into the co-evolution of these closely interacting clusters.

Acknowledgements We thank the anonymous referee for the constructive comments and suggestions that helped improve the quality of this manuscript. This study has been supported in part by the Scientific and Technological Research Council (TÜBİTAK) 122F109. This work presents results from the European Space Agency (ESA) space mission *Gaia*. *Gaia* data are being processed by the *Gaia* Data Processing and Analyzis Consortium (DPAC). Funding for the DPAC is provided by national institutions, in particular, the institutions participating in the *Gaia* Multi-Lateral Agreement (MLA). The *Gaia* mission website is <https://www.cosmos.esa.int/gaia>. The *Gaia* archive website is <https://archives.esac.esa.int/gaia>. The authors would like to express their gratitude to the Deanship of Scientific Research at Northern Border University, Arar, KSA, for funding this research under project number "NBU-FFR-2026-237-02".

References

Adams, F. C., & Myers, P. C. 2001, ApJ, 553, 744 29

Ak, T., Bostancı, Z. F., Yontan, T., et al. 2016, Astrophysics and Space Science, 361, 126 12

Akbaba, F., Ak, T., Bilir, S., et al. 2024, Astronomische Nachrichten, 345, e20240052 23

Akulut, B., Ak, S., Yontan, T., et al. 2021, Astrophysics and Space Science, 366, 68 8

Allison, R. J., Goodwin, S. P., Parker, R. J., et al. 2009, ApJ, 700, L99 30

Alzhrani, A. Y., Haroon, A. A., Elsanhoury, W. H., & Çınar, D. C. 2025, Journal of Astrophysics and Astronomy, 46, 50 16

Bailer-Jones, C. A. L., Rybizki, J., Fouesneau, M., Demleitner, M., & Andrae, R. 2021, AJ, 161, 147 16

Bailer-Jones, C. A. L., Rybizki, J., Fouesneau, M., Mantelet, G., & Andrae, R. 2018, AJ, 156, 58 15

Banks, T., Yontan, T., Bilir, S., & Canbay, R. 2020, Journal of Astrophysics and Astronomy, 41, 6 12

Bica, E., & Bonatto, C. 2005, A&A, 443, 465 6, 7

Bilir, S., Güver, T., & Aslan, M. 2006, Astronomische Nachrichten, 327, 693 11

Bilir, S., Güver, T., Khamitov, I., et al. 2010, Astrophysics and Space Science, 326, 139 12

Bilir, S., Karaali, S., Ak, S., et al. 2012, MNRAS, 421, 3362 20

Bilir, S., Bostancı, Z. F., Yontan, T., et al. 2016, Advances in Space Research, 58, 1900 12

Bisht, D., Jiang, I.-G., Elsanhoury, W. H., et al. 2026, AJ, 171, 72 16

Bonatto, C., & Bica, E. 2005, A&A, 437, 483 6, 7

Bonnell, I. A., Bate, M. R., & Zinnecker, H. 1998, MNRAS, 298, 93 30

Boss, A. P., & Keiser, S. A. 2012, ApJ, 756, L9 31

Bostancı, Z. F., Ak, T., Yontan, T., et al. 2015, MNRAS, 453, 1095 12

Bostancı, Z. F., Yontan, T., Bilir, S., et al. 2018, Ap&SS, 363, 143 12

Bovy, J. 2015, ApJS, 216, 29 18, 19

Bragaglia, A., Carretta, E., Gratton, R. G., et al. 2001, AJ, 121, 327 2

Bragg, A. E., & Kenyon, S. J. 2005, AJ, 130, 134 31

Bressan, A., Marigo, P., Girardi, L., et al. 2012, MNRAS, 427, 127 12, 13, 14, 27

Camargo, D. 2021, ApJ, 923, 21 2

Camargo, D., Bonatto, C., & Bica, E. 2010, A&A, 521, A42 7

Canbay, R., Ak, T., Bilir, S., Soydugan, F., & Eker, Z. 2025, AJ, 169, 87 23

Canbay, R., Bilir, S., Özgünmez, A., & Ak, T. 2023, AJ, 165, 163 13, 14

Cantat-Gaudin, T., Jordi, C., Vallenari, A., et al. 2018a, A&A, 618, A93 8

Cantat-Gaudin, T., Jordi, C., Vallenari, A., et al. 2018b, A&A, 618, A93 31

Cantat-Gaudin, T., Anders, F., Castro-Ginard, A., et al. 2020, A&A, 640, A1 2, 8, 10, 11, 15, 19

Cappa, C., Niemela, V., & Herbstmeier, U. 1996, in Revista Mexicana de Astronomia y Astrofisica Conference Series, Vol. 4, Revista Mexicana de Astronomia y Astrofisica Conference Series, ed. E. Falco, J. A. Fernandez, & R. F. Ferrero, 83 32

Cardelli, J. A., Clayton, G. C., & Mathis, J. S. 1989, ApJ, 345, 245 17

Carrera, R., Casamiquela, L., Bragaglia, A., et al. 2022, A&A, 663, A148 19

Castelli, F., & Kurucz, R. L. 2003, in Modelling of Stellar Atmospheres, Vol. 210, A20 16

Castro-Ginard, A., Jordi, C., Luri, X., et al. 2018, A&A, 618, A59 8

Castro-Ginard, A., Penoyre, Z., Casey, A. R., et al. 2024, A&A, 688, A1 3

Çakmak, H., Yontan, T., Bilir, S., et al. 2024, Astronomische Nachrichten, 345, e20240054 14

Çınar, D. C., Bilir, S., Şahin, T., & Plevne, O. 2025, AJ, 170, 13 23

Çınar, D. C., Taşdemir, S., Koç, S., & Iyer, S. 2024, Physics and Astronomy Reports, 2, 1 23

Chupina, N., Reva, V., & Vereshchagin, S. 2001, A&A, 371, 115 22

Chupina, N. V., Reva, V. G., & Vereshchagin, S. V. 2006, A&A, 451, 909 22

Coşkunoğlu, B., Ak, S., Bilir, S., et al. 2012, MNRAS, 419, 2844 20

Coşkunoğlu, B., Ak, S., Bilir, S., et al. 2011, MNRAS, 412, 1237 20

Currie, T., Hernandez, J., Irwin, J., et al. 2010, ApJS, 186, 191 2, 30, 31, 32

de La Fuente Marcos, R., & de La Fuente Marcos, C. 2009, *A&A*, 500, L13 2

Dias, W. S., Monteir, H., Moitinho, A., et al. 2021, *MNRAS*, 504, 356 11, 15

Döner, S., Ak, S., Önal Taş, Ö., & Plevne, O. 2023, *Physics and Astronomy Reports*, 1, 11 20

Elsanhouri, W. H. 2016, *Astrophysics*, 59, 246 22

Elsanhouri, W. H. 2025, *Astronomische Nachrichten*, 346, e20240082 22

Elsanhouri, W. H., & Amin, M. Y. 2019, *Serbian Astronomical Journal*, 198, 45 22

Elsanhouri, W. H., Haroon, A. A., Elkholly, E. A., & Çınar, D. C. 2025a, *Journal of Astrophysics and Astronomy*, 46, 21 22

Elsanhouri, W. H., Tasdemir, S., Çınar, D. C., et al. 2025b, arXiv e-prints, arXiv:2601.00061 22

Elsanhouri, W., Postnikova, E., Chupina, N., et al. 2018, *Astrophysics and Space Science*, 363, 1 22

Fellhauer, M., & Kroupa, P. 2005, *MNRAS*, 359, 223–228 31

Fitzpatrick, E. L. 1999, *PASP*, 111, 63 16

Foreman-Mackey, D., Hogg, D. W., Lang, D., & Goodman, J. 2013, *PASP*, 125, 306 12

Fujimoto, M., & Kumai, Y. 1997, *AJ*, 113, 249 2

Fujimoto, M. Y., & Kumai, Y. 1997, *ApJ*, 404, 497–503 31

Gaia Collaboration, Prusti, T., de Bruijne, J. H. J., et al. 2016, *A&A*, 595, A1 2

Gaia Collaboration, Brown, A. G. A., Vallenari, A., et al. 2018, *A&A*, 616, A1 19, 21

Gaia Collaboration, Vallenari, A., Brown, A. G. A., et al. 2023, *A&A*, 674, A1 3, 16, 19

Gokmen, S., Eker, Z., Yontan, T., et al. 2023, *AJ*, 166, 263 14

GRAVITY Collaboration, Abuter, R., Amorim, A., et al. 2018, *A&A*, 615, L15 18

Haroon, A. A., Elsanhouri, W. H., Elkholly, E. A., Saad, A. S., & Çınar, D. C. 2025, *Physica Scripta*, 100, 055006 22

Haroon, A. A., Elsanhouri, W. H., Saad, A. S., & Elkholly, E. A. 2024, *Contributions of the Astronomical Observatory Skalnate Pleso*, 54, 22 2

Hasan, P., & Hasan, S. 2011, arXiv:1101.2178 26

Higson, E., Handley, W., Hobson, M., & Lasenby, A. 2019, *Statistics and Computing*, 29, 891 16

Hill, A., & Zaritsky, D. 2006, *AJ*, 131, 414 7

Hillenbrand, L. A., & Hartmann, L. W. 1998, *ApJ*, 492, 540 30

Horie, S., Okamoto, T., & Habe, A. 2024, *MNRAS*, 527, 10077 31

Hunt, E. L., & Reffert, S. 2023, *A&A*, 673, A114 19

Hunt, E. L., & Reffert, S. 2024, *A&A*, 686, A42 10, 11, 15

Husser, T. O., Wende-von Berg, S., Dreizler, S., et al. 2013, *A&A*, 553, A6 16

Iffrig, O., & Hennebelle, P. 2015, *A&A*, 576, A95 31

Johnson, D. R. H., & Soderblom, D. R. 1987, *AJ*, 93, 864 20

Karagöz, H., Yontan, T., Bilir, S., et al. 2025, *AJ*, 170, 149 8

Kharchenko, N. V., Piskunov, A. E., Schilbach, E., Röser, S., & Scholz, R.-D. 2013, *A&A*, 558, A53 7

King, I. 1962, *AJ*, 67, 471 6

King, I. R. 1966, *AJ*, 71, 64 7

Koç, S., Yontan, T., Bilir, S., et al. 2022, *AJ*, 163, 191 12

Krone-Martins, A., & Moitinho, A. 2014, A&A, 561, A57 8

Leggett, S. K. 1992, ApJS, 82, 351 21

Li, Z., & Zhu, Z. 2025, A&A, 700, A280 2

Lindegren, L., Bastian, U., Biermann, M., et al. 2021, A&A, 649, A4 3

Marco, A., Bernabeu, G., & Negueruela, I. 2001, AJ, 121, 2075 2

Marshall, D. J., Robin, A. C., Reylé, C., Schultheis, M., & Picaud, S. 2006, A&A, 453, 635 5

McDonald, I., Zijlstra, A. A., & Watson, R. A. 2017, MNRAS, 471, 770–797 31

McMillan, S. L. W., Vesperini, E., & Portegies Zwart, S. F. 2007, ApJ, 655, L45 30

Miocchi, P., Lanzoni, B., Ferraro, F. R., et al. 2013, ApJ, 774, 151 7

Miyamoto, M., & Nagai, R. 1975, Publications of the Astronomical Society of Japan, 27, 533 18

Muñoz, R. R., Geha, M., & Willman, B. 2010, AJ, 140, 138 7

Navarro, J. F., Frenk, C. S., & White, S. D. M. 1996, ApJ, 462, 563 18

Palma, T., Coenda, V., Baume, G., & Feinstein, C. 2025, A&A, 693, A218 2

Parker, R. J., Goodwin, S. P., Wright, N. J., Meyer, M. R., & Quanz, S. P. 2016, MNRAS, 459, L119 30

Pecaut, M. J., & Mamajek, E. E. 2013, ApJS, 208, 9 13

Piatti, A. E., & Malhan, K. 2022, MNRAS, 511, L1 24, 31

Piskunov, A. E., Schilbach, E., Kharchenko, N. V., Röser, S., & Scholz, R.-D. 2007, A&A, 468, 151 7

Plevne, O., Önal Taş, Ö., Bilir, S., & Seabroke, G. M. 2020, ApJ, 893, 108 15

Reid, M. J., Pesce, D. W., & Riess, A. G. 2019, ApJ, 886, L27 32

Riello, M., De Angeli, F., Evans, D. W., et al. 2021, A&A, 649, A3 5

Robin, A. C., Reylé, C., Derrière, S., & Picaud, S. 2003, A&A, 409, 523 5

Ruprecht, J. 1966, Bulletin of the Astronomical Institutes of Czechoslovakia, 17, 33 2

Salpeter, E. E. 1955, ApJ, 121, 161 26, 27

Schlafly, E. F., & Finkbeiner, D. P. 2011, ApJ, 737, 103 16, 31

Sharma, S., Pandey, A. K., Ogura, K., et al. 2008, AJ, 135, 1934 26

Skrutskie, M. F., Cutri, R. M., Stiening, R., et al. 2006, AJ, 131, 1163 16

Slesnick, C. L., Hillenbrand, L. A., & Massey, P. 2002a, ApJ, 576, 880 26

Slesnick, C. L., Hillenbrand, L. A., & Massey, P. 2002b, ApJ, 576, 880 31, 32

Song, F., Esamdin, A., Hu, Q., & Zhang, M. 2022, A&A, 666, A75 2, 15

Soubiran, C., Cantat-Gaudin, T., Romero-Gómez, M., et al. 2018, A&A, 619, A155 19, 21

Speagle, J. S. 2020, MNRAS, 493, 3132 16

Spitzer, Jr., L., & Hart, M. H. 1971, ApJ, 166, 483 28

Taşdemir, S., & Çınar, D. C. 2025, Contributions of the Astronomical Observatory Skalnaté Pleso, 55, 506 2

Taşdemir, S., Çınar, D. C., Canbay, R., et al. 2025, Physics and Astronomy Reports, 3, 1 23

Taşdemir, S., & Yontan, T. 2023, Physics and Astronomy Reports, 1, 1 23

Tanık Öztürk, B., Bilir, S., Yontan, T., et al. 2025, AJ, 170, 164 12

Tarricq, Y., C., S., Casamiquela, L., et al. 2021, A&A, 647, A19 19

Tsantaki, M., Pancino, E., Marrese, P., et al. 2022, A&A, 659, A95 19

Tunçel Güçtekin, S., Bilir, S., Karaali, S., Plevne, O., & Ak, S. 2019, *Advances in Space Research*, 63, 1360 18

Vereshchagin, S. V., Tutukov, A. V., Chupina, N. V., Postnikova, E. S., & Sizova, M. D. 2022, *Astronomy Reports*, 66, 361 2

Vines, J. I., & Jenkins, J. S. 2022, *MNRAS*, 513, 2719 16

Šablevičiūtė, I., Vansevičius, V., Kodaira, K., et al. 2006, *Baltic Astronomy*, 15, 547 28

Wang, H., Zhang, Y., Zeng, X., et al. 2022, *AJ*, 164, 40 8

Wright, E. L., Eisenhardt, P. R. M., Mainzer, A. K., et al. 2010, *AJ*, 140, 1868 16

Yontan, T. 2023, *AJ*, 165, 79 8

Yontan, T., Bilir, S., Çakmak, H., et al. 2023, *Advances in Space Research*, 72, 1454 14, 21

Yontan, T., & Canbay, R. 2023, *Physics and Astronomy Reports*, 1, 65 14

Yontan, T., Bilir, S., Bostancı, Z. F., et al. 2015, *Astrophysics and Space Science*, 355, 267 12

Yontan, T., Bilir, S., Bostancı, Z. F., et al. 2019, *Astrophysics and Space Science*, 364, 152 12

Yontan, T., Bilir, S., Ak, T., et al. 2021, *Astronomische Nachrichten*, 342, 538 8

Yontan, T., Çakmak, T., Bilir, S., et al. 2022, *Revista Mexicana de Astronomia y Astrofisica Conference Series*, 58, 333 8

Yücel, G., Canbay, R., & Bakış, V. 2024, *Physics and Astronomy Reports*, 2, 18 23

Zhong, J., Chen, L., Wu, D., et al. 2020, *A&A*, 640, A127 15